Applied Ocean Research 175 (2026) 105202

Contents lists available at ScienceDirect

Applied Ocean Research

journal homepage: www.elsevier.com/locate/apor

Research paper

Simulink toolbox for the analysis of oscillating-water-column wave energy converters using the WEC-Sim simulator

A.A.D. Carrelhas, L.M.C. Gato *, C.G. Cartaxo

IDMEC, Instituto Superior Técnico, Universidade de Lisboa, Av. Rovisco Pais 1, 1049-001 Lisboa, Portugal

ARTICLE INFO

Keywords:
Wave energy
Oscillating water column
WEC-Sim
Turbine generator control
Air compressibility

ABSTRACT

The WEC-Sim is an open-source simulation tool for wave energy converters (WECs), developed in MATLAB/Simulink using the multi-body dynamics solver SimMechanics. This tool has been utilised to model both floating and submerged oscillating body WECs, as well as power take-off (PTO) and mooring systems. The paper describes the mathematical modelling implemented in a novel Simulink toolbox that enables the analysis of oscillating-water-column (OWC) WECs using the WEC-Sim tool. The new WEC-Sim Simulink OWC model addresses the mass balance of the OWC system by considering the thermodynamics of the air within the pneumatic chamber, the flow through both linear and non-linear turbines, and the use of safety valves arranged either in series or parallel with the turbine. It also incorporates the electrical generator and the control system for the PTO. An OWC device integrated into a breakwater was chosen as the test case to compare the results from WEC-Sim with those from an in-house frequency-domain numerical model based on linear potential flow theory. This comparison aims to assess the accuracy of the mathematical model and demonstrate the capabilities of the numerical method. Results indicate that the WEC-Sim tool can be easily adapted to accurately compute the dynamics of OWC-type WECs, taking into account air compressibility in the pneumatic chamber, linear and non-linear turbines, air valves in both series and parallel configurations with the turbine, electrical generators, and the control of the turbine-generator setup, under various sea states, whether high or low energy.

1. Introduction

Unlike mainstream renewable energy technologies, which represent a significant share in a considerable number of countries, wave energy remains uncompetitive. Besides the inherent difficulty of implementing such technology in a harsh environment, there is a wide variety of wave energy conversion technologies. These include oscillating bodies (Gomes et al., 2015; Cheng et al., 2024, 2026), oscillating water column (OWC) (Falcão et al., 2020; Hu et al., 2026; Cheng et al., 2022), over-topping (Tedd and Kofoed, 2009) and membrane pump devices (Ryan et al., 2015). Reviews of the technology are presented in Refs. (Falcão, 2010; Uihlein and Magagna, 2016).

OWC devices are considered among the most reliable WECs because the only moving parts are the rotors of the air turbine and the electrical generator, which are located above the water's surface (Carrelhas et al., 2019). The principle of operation is simple. OWC devices comprise a fixed or floating hollow structure, referred to as the air chamber, which is open to the sea below the water surface and holds air above the inner free surface. The action of the waves alternately compresses and decompresses the air confined in the chamber. The pressure differential between the air chamber and the atmosphere drives a self-rectifying air turbine.

Several closed-source computer programs based on linear wave potential flow theory were developed and used to design and analyse bottom-fixed and floating OWC WECs (Gomes et al., 2020; Scialò et al., 2021; Iturrioz et al., 2014). Dependence on exclusively closed-source software presents significant challenges to scientific rigour and community advancement. Open-source software effectively addresses these challenges by facilitating inspectable, reviewable, and auditable implementations, thereby enhancing verification and validation practices and promoting reproducible research. The WEC-Sim is an open-source time-domain simulation tool developed in MATLAB/Simulink for simulating WECs using the multi-body dynamics solver SimMechanics and linear wave potential flow theory (Ruehl et al., 2023). The software was developed in collaboration between Oregon State University (OSU), National Renewable Energy Laboratory (NREL) and Sandia National Laboratories (Sandia). The flexibility of the WEC-Sim software allows easy adaptation to different needs within the wave energy industry. The

* Corresponding author.
E-mail address: luis.gato@tecnico.ulisboa.pt (L.M.C. Gato).

https://doi.org/10.1016/j.apor.2026.105202
Received 2 October 2025; Received in revised form 7 March 2026; Accepted 26 July 2026
Available online 28 August 2026

Nomenclature

Romans

a_{RO}	control law parameter [Nms^b]
A	added mass [kg]
b	control law parameter [-]
b_1	converter length [m]
B	radiation force coefficient [kg/s]
D	turbine rotor diameter [m]
f_e, f_r, f_p, f_b	excitation, radiation, piston, net hydrostatic restoring force [N]
F_e F_r F_p F_b	complex amplitude of f_e, f_r, f_p, f_b [N]
g	gravity acceleration [m/s^2]
g_r	memory function (Eq. (30)) [N/m]
H_s	significant wave height [m]
I	inertia [kgm^2]
k_L	linear turbine constant [ms]
k_N	non-linear turbine constant [kg$^{1/2}$m$^{1/2}$]
K_L	linear turbine coefficient [-]
K_N	non-linear turbine coefficient [-]
l_0	air chamber height in calm water [m]
m	air mass in the pneumatic chamber [kg]
m_p	piston mass [kg]
n	polytropic index [-]
p_a	atmospheric pressure [Pa]
p_c	air chamber pressure relative to the atmosphere [Pa]
p_{sv}	series valve pressure drop [Pa]
p_t	turbine pressure head [Pa]
$\mathcal{P}$	complex amplitude of p_c [Pa]
P_a	turbine available power [W]
P_g	electrical generator power [W]
P_t	turbine shaft power [W]
P_w	wave power per unit wave crest length [W/m]
q	volume flow rate displaced by the free surface oscillation [m^3/s]
q_t	turbine volume flow rate [m^3/s]
Q	complex amplitude of q [m^3/s]
S	inner free-surface area [m^2]
S_{bv}	bypass valve passage area [m^2]
S_{sv}	series valve passage area [m^2]
S_ω	energy density spectrum [m^{2}s]
t	time [s]
T, T_e, T_p	regular wave, energy, peak period [s]
T_g	generator electromagnetic torque [Nm]
T_t	turbine shaft torque [Nm]
u	valve shutter position [-, °]
V	air chamber volume [m^3]
V_0	air chamber volume in calm water [m^3]
w_{bv}	bypass valve mass flow rate [kg/s]
w_t	turbine mass flow rate [kg/s]
z	vertical coordinate [m]
Z	complex amplitude of z [m]

Greek symbols

α	argument of F_e [rad]
Δt	time step, time interval [s]
Λ	complex constant in Eq. (13) [-]
Π	power (torque) coefficient [-]
ρ_a, ρ_c, ρ_{ref}	atmospheric, pneumatic chamber, reference air density [kg/m^3]
ρ_w	sea water density [kg/m^3]
Φ	flow rate coefficient [-]
Ψ	pressure head coefficient [-]
ω	radian frequency [rad/s]
Ω	rotational speed [rad/s]
Γ	Excitation force complex amplitude per unit of wave amplitude [N/m]
σ	standard deviation (or rms)
ξ	head loss coefficient [-]

Subscripts

CIC	with reference to convolution integral
CL, CLV	with reference to control law
max	maximum value
L	lower threshold value
rated	rated value
ref	reference value
Sim	WEC-Sim solution value
thrs, thrsV	threshold value
U	upper threshold value

Superscripts

max	maximum value
min	minimum value
rated	rated value
RO	regular operation
SM	safe mode
SMV	safe mode with valve
*	normalised value
–	time averaged value

Acronyms

BEM	boundary element method
OWC	oscillating water column
PTO	power take-off system
RO	regular operation
SM	safe mode
WEC	wave energy converter

tool is popular in the wave energy community, both academic and industrial, since it provides a framework to model floating and submerge oscillating rigid body WECs, including non-linear hydrodynamic effects, power take-off (PTO), PTO control and mooring systems (Ruehl et al., 2023). In a preliminary phase of geometry optimisation, for example, the linear wave potential flow models are suitable and accurate (Fox et al., 2021). Another advantage is its calculation time, which is orders of magnitude faster compared to computational fluid dynamics (CFD) models.

Two comprehensive approaches are adopted in the modelling of OWCs: the piston model and the free-surface model. In the first, the OWC inner surface is simulated by a heaving weightless piston, with added mass, $A(\omega)$, radiation force coefficient, $B(\omega)$, and excitation force complex amplitude, $F_e(\omega)$, computed with the boundary element method (BEM) codes used for oscillating bodies such as the WAMIT (Lee and Newman, 2021), NEMOH (Kurnia and Ducrozet, 2021) and Capytaine (Ancellin and Dias, 2019). In the free-surface model, the equations are expressed in terms of the OWC free surface

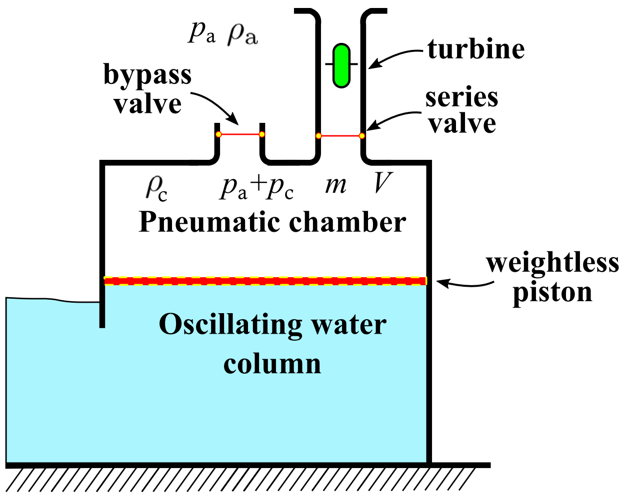

Fig. 1. Fixed-structure OWC WEC with air turbine and bypass and throttle valves: piston model.
Source: Adapted from Falcão and Justino (1999).

pressure and flow rate displaced by its motion, being the set of the corresponding hydrodynamic coefficients, radiation conductance, $G(\omega)$, radiation susceptance, $H(\omega)$, and excitation flow rate complex amplitude, $Q_e(\omega)$ related to the set $A(\omega)$, $B(\omega)$, $F_e(\omega)$ of the piston model (Falcão and Henriques, 2016). The piston model better fits the WEC-Sim modelling, Fig. 1. Modelling OWC WECs couples: (1) hydrodynamics, (2) the effect of compressibility of the OWC air chamber (Falcão and Justino, 1999) and (3) turbine damping as function of the rotational speed. A simplified WEC-Sim OWC modelling approach (So et al., 2020) and the computation of non-linear Froude–Krylov forces on a spar buoy (Giorgi et al., 2021) with WEC-Sim have been published.

To the authors' knowledge, there has been no published WEC-Sim implementation example that fully models an fixed-structure OWC WEC. Additionally, a systematic validation procedure or validation for all turbine types and air valves has not been established. To address the lack of inherent OWC functionality in WEC-Sim, a Simulink model block is presented. It incorporates key pneumatic and electromechanical subsystems, including air compressibility in the pneumatic chamber, air turbines, air valves in series and parallel with the turbine, electrical generators, and control of the turbine-generator set. The fundamental formulations and their integration into usable Simulink blocks are presented and analysed, facilitating thorough OWC evaluations inside the WEC-Sim framework. An OWC device configuration integrated into a caisson breakwater was considered as test case to compare the WEC-Sim results with those of in-house frequency-domain numerical model based on linear wave potential flow theory.

The research question is: Could a modular Simulink/WEC-Sim toolbox simulate OWC hydrodynamic, pneumatic, and electromechanical interaction and predict power and load at a competitive computational cost?

The main contributions of the paper are:

- Validation of the new Simulink WEC-SIM model by cross-checking it with an in-house code.
- Public, integrated, and validated OWC toolbox in WEC-Sim that makes it possible to use key OWC physics, PTO dynamics (turbine/valves), and generator-control coupling in a Simulink workflow.
- Development of a standard, reproducible benchmarking procedure for numerical simulation of fixed OWC WECs.

The structure of the paper is as follows. The fixed-structure OWC WEC modelling as implemented in the used in-house numerical model is presented in Section 2. The new Simulink blocks that enable the analysis of fixed-structure OWC WECs with the WEC-Sim code are described in Section 3. Section 4 presents the test case and the corresponding hydrodynamic coefficients. Frequency domain and time-domain results, considering regular and irregular waves and linear and non-linear turbines, are summarised in Section 5. The main findings of the paper are presented in Section 6.

2. Theoretical model

This Section describes the piston model for a fixed-structure OWC WEC as implemented in the in-house code and in the present WEC-Sim formulation.

Heave is the only motion mode present in the piston modelling of fixed-structure OWC WEC of interest. Therefore, the analysis considers only the heave motion. The coordinate system assumes the wave propagates in the positive x-axis direction and that the piston heave motion is positive vertically in the upward direction of the z-axis. Newton's second law gives the governing equation for the piston motion of the fixed-structure OWC WEC as

$$m_p \frac{d^2 z(t)}{dt^2} = f_e(t) + f_r(t) + f_p(t) + f_b(t) , \tag{1}$$

where m_p is the piston mass, t is time, $z(t)$ is the piston displacement, $f_e(t)$ is the force actuating on the piston resulting from the incident wave excitation, $f_r(t)$ is the wave radiation force due to the piston displacement, $f_p(t)$ is the pressure force on the piston resulting from the air pressure oscillation in the pneumatic chamber and $f_b(t)$ is the piston net hydrostatic restoring force.

The excitation, $f_e(t)$, and the radiation, $f_r(t)$, forces are calculated from the hydrodynamic coefficients computed by a BEM code (Lee and Newman, 2021; Kurnia and Ducrozet, 2021; Ancellin and Dias, 2019) for the given fixed-structure OWC WEC.

2.1. Air chamber mass balance

Consider an OWC pneumatic chamber with volume V_0 in the absence of incident waves, an air turbine placed in a duct between the air chamber and the atmosphere, and a valve in series and or in parallel (bypass) with the turbine, as depicted in Fig. 1. The free surface oscillates by the action of the waves, displacing a volume flow rate (negative for downward motion)

$$q(t) = -\frac{dV(t)}{dt} , \tag{2}$$

where $V(t)$ is the instantaneous air chamber volume. Therefore, the instantaneous air mass inside the pneumatic chamber is given by

$$m(t) = \rho_c(t) V(t) , \tag{3}$$

where $\rho_c(t)$ is the air density inside the chamber which changes with time due to the air compressibility.

The time variation of the mass of air inside the chamber equals the negative of the sum of the turbine mass flow rate $w_t(t)$ and the mass flow rate through the bypass valve $w_{bv}(t)$, both positive for air flowing out of the chamber.

$$-\frac{dm(t)}{dt} = w_t(t) + w_{bv}(t) . \tag{4}$$

From Eqs. (3) and (4), comes

$$w_t(t) + w_{bv}(t) = -V(t)\frac{d\rho_c(t)}{dt} + \rho_c(t) q(t) . \tag{5}$$

The increase or decrease of the air volume inside the OWC pneumatic chamber is assumed to be a polytropic process with index n (Falcão and Justino, 1999; Falcão and Henriques, 2014, 2019). Then, it is

$$\frac{p_c(t) + p_a}{\rho_c^n(t)} = \frac{p_a}{\rho_a^n} , \tag{6}$$

where $p_c(t)$ and $\rho_c(t)$ are the internal air pressure oscillation relative to the atmosphere and density, p_a and ρ_a are the atmospheric air pressure and density. Therefore, the derivative $\mathrm{d}\rho_c(t)/\mathrm{d}t$ is related to $\mathrm{d}p_c(t)/\mathrm{d}t$ through

$$\frac{\mathrm{d}\rho_c(t)}{\mathrm{d}t} = \frac{\rho_c(t)}{n(p_c(t)+p_a)}\frac{\mathrm{d}p_c(t)}{\mathrm{d}t}\,. \tag{7}$$

From Eq. (5), the mass balance of air inside the chamber is written as

$$q(t) = \frac{w_t(t)+w_{bv}(t)}{\rho_a}\left(\frac{p_a}{p_c(t)+p_a}\right)^{1/n} + \frac{V(t)}{n(p_c(t)+p_a)}\frac{\mathrm{d}p_c(t)}{\mathrm{d}t}\,. \tag{8}$$

The frequency domain model analysis is first introduced, considering small-amplitude regular waves, a linear turbine, and no valves. Then, the time domain model is described, considering both regular and irregular waves, as well as linear and non-linear turbines, and air valves operating in series or parallel with the turbine.

2.2. OWC piston model frequency-domain analysis

Assuming small pressure oscillations it is $p_c(t) \ll p_a$ and $|V(t)-V_0| \ll V_0$. Further supposing no valves, Eq. (8) becomes

$$q(t) = \frac{w_t(t)}{\rho_a} + \frac{V_0}{np_a}\frac{\mathrm{d}p_c(t)}{\mathrm{d}t}\,. \tag{9}$$

For the frequency-domain analysis to be applicable, the turbine is assumed to be linear for the system to be fully linear, i.e.

$$w_t(t) = k_L p_c(t)\,. \tag{10}$$

Substituting Eq. (10) in Eq. (9) gives

$$q(t) = k_L p_c(t) + \frac{V_0}{np_a}\frac{\mathrm{d}p_c(t)}{\mathrm{d}t}\,. \tag{11}$$

Supposing the system to be linear and subjected to regular incident waves with frequency ω, the piston displacement, $z(t)$, the air pressure oscillation, $p_c(t)$, the air volume flow rate, $q(t)$, the incident wave excitation force, $f_e(t)$, the radiation force, $f_r(t)$, the piston pressure force, $f_p(t)$, and the piston hydrostatic restoring force, $f_b(t)$, are harmonic functions with the same frequency. Using the complex representation of harmonic oscillations, it is

$$\begin{aligned}\{z, p_c, q, f_e, f_r, f_p, f_b\}(t) &= \\ &= \mathrm{Re}[\{Z, \mathcal{P}, Q, F_e, F_r, F_p, F_b\}(\omega)\exp \mathrm{i}\omega t]\end{aligned} \tag{12}$$

where, $Z(\omega)$, $\mathcal{P}(\omega)$, $Q(\omega)$, $F_e(\omega)$, $F_r(\omega)$, $F_p(\omega)$ and $F_b(\omega)$ are the complex amplitudes of the body displacement, air pressure oscillation, volume flow rate displaced by the free surface, incident wave excitation force, the piston radiation force, the pressure force on the piston and the piston net hydrostatic restoring force, respectively. In the frequency domain, Eq. (11) becomes

$$Q(\omega) = \Lambda^{-1}(\omega)\mathcal{P}(\omega)\,, \tag{13}$$

where

$$\Lambda(\omega) = \left(k_L + \frac{\mathrm{i}\omega V_0}{np_a}\right)^{-1}\,. \tag{14}$$

From Eq. (2), the volume flow rate displaced by the free-surface oscillation is

$$q(t) = \mathrm{Re}[\mathrm{i}\omega S Z(\omega)\exp \mathrm{i}\omega t]\,, \tag{15}$$

where S is the piston wet (OWC free surface) area. Then

$$Q(\omega) = \mathrm{i}\omega S Z(\omega)\,, \tag{16}$$

and

$$\mathcal{P}(\omega) = \mathrm{i}\omega S\Lambda(\omega)Z(\omega)\,. \tag{17}$$

Following Evans's decomposition (Evans, 1982), it is convenient to write the radiation force complex amplitude on the piston as

$$F_r(\omega) = (\omega^2\, A(\omega) - \mathrm{i}\omega B(\omega))Z(\omega)\,, \tag{18}$$

where $A(\omega)$ and $B(\omega)$ are the piston added mass and radiation force coefficient, which are functions of the OWC geometry and the frequency ω. The pressure force on the piston and the piston net hydrostatic restoring force complex amplitudes are

$$F_p(\omega) = \mathrm{i}\omega S^2\Lambda(\omega)Z(\omega) \tag{19}$$

and

$$F_b(\omega) = -\rho_w g S Z(\omega)\,, \tag{20}$$

respectively, where ρ_w is the sea-water density and g is the gravity acceleration. The excitation force complex amplitude $F_e(\omega)$ is obtained from the excitation force complex amplitude per unit incident wave amplitude $\Gamma(\omega)$ computed by a BEM code for the fixed-structure OWC WEC as

$$F_e(\omega) = \Gamma(\omega)A_w\,. \tag{21}$$

Therefore, in the frequency domain, Eq. (1) can be written as

$$\left(-\omega^2(m_p + A(\omega)) + \rho_w g S + \mathrm{i}\omega(B(\omega) + \Lambda(\omega)S^2)\right) Z(\omega) = F_e(\omega)\,, \tag{22}$$

if we get rid of time. The time-averaged available pneumatic power to the turbine is then

$$\bar{P}_a(\omega) = \frac{1}{2}k_L|\mathcal{P}(\omega)|^2\,. \tag{23}$$

2.3. OWC piston model time-domain analysis

Time-domain analysis is necessary when wave amplitudes are significant, or the turbine flow rate exhibits a non-linear relationship with pressure. In that case, the linearisation described in Section 2.2 is unnecessary. The air chamber volume is then written as

$$V(t) = V_0 - Sz(t)\,, \tag{24}$$

and the mass balance (Eq. (8)) as

$$\begin{aligned} S\frac{\mathrm{d}z(t)}{\mathrm{d}t} = \frac{w_t(t)+w_{bv}(t)}{\rho_a}\left(\frac{p_a}{p_c(t)+p_a}\right)^{1/n} &+ \\ + \frac{V_0 - Sz(t)}{n(p_c(t)+p_a)}\frac{\mathrm{d}p_c(t)}{\mathrm{d}t}&\,,\end{aligned} \tag{25}$$

where $w_t(t)$ is given by Eq. (10) if the turbine is assumed linear, or by any function

$$w_t(t) = f(p_c(t))\,, \tag{26}$$

if the turbine is non-linear, or the plant is equipped with a safety valve in series with the turbine.

The piston and buoyancy force terms on Eq. (1) can be expressed as

$$f_p(t) = Sp_c(t) \tag{27}$$

and

$$f_b(t) = -\rho_w g S z(t)\,. \tag{28}$$

In the time domain, the radiation force is expressed using a convolution integral (Cummins, 1962) that captures the fluid memory effect as

$$f_r(t) = -A(\infty)\frac{\mathrm{d}^2 z(t)}{\mathrm{d}t^2} - \int_0^t g_r(t-\tau)\frac{\mathrm{d}z(\tau)}{\mathrm{d}\tau}\mathrm{d}\tau\,, \tag{29}$$

where $A(\infty)$ is the piston added mass at infinite wave frequency and the radiation force term memory function $g_r(t)$ is the response upon application of an input impulse at $t = 0$, assuming $p_c(t) = 0$ for $t \leq 0$, defined as

$$g_r(t) = \frac{2}{\pi}\int_0^\infty B(\omega)\cos(\omega t)\mathrm{d}\omega\,. \tag{30}$$

Then, Eq. (1) can be written as

$$\begin{aligned}(m_p + A(\infty))\frac{\mathrm{d}^2 z(t)}{\mathrm{d}t^2} &= f_e(t) - \\ &- \int_0^t g_r(t-\tau)\frac{\mathrm{d}z(\tau)}{\mathrm{d}\tau}\mathrm{d}\tau - \rho_w g S z(t) - Sp_c(t)\,.\end{aligned} \tag{31}$$

For regular waves the excitation force is

$$f_e(t) = \mathrm{Re}[F_e(\omega)\exp(\mathrm{i}\omega t)] = |\Gamma(\omega)| A_w \cos(\omega t + \alpha(\omega)), \tag{32}$$

where $\alpha(\omega)$ is the phase of the excitation force of amplitude $F_e(\omega)$.

Irregular waves are conveniently described by a superposition of a finite number of sinusoidal waves with different amplitudes and frequencies with the energy distribution given by a energy density spectrum $S_\omega(\omega)$ (Holthuijsen, 2007), characterised by a significant wave height H_s and a peak or energy period, T_p or T_e, respectively. Therefore, the excitation force due to incident irregular waves can be described as

$$f_e(t) = \mathrm{Re}\left[\sum_{i=1}^{N} |\Gamma(\bar{\omega}_i)| A_{\omega,i} \exp[\mathrm{i}(\bar{\omega}_i t + \alpha_i)]\right], \tag{33}$$

where N is the number of frequency bands $\omega_i \le \omega \le \omega_{i+1}$ of width $\delta_i = \omega_{i+1} - \omega_i$ chosen to discretise the spectrum,

$$A_{\omega,i} = (2S_\omega(\bar{\omega}_i)\delta_i)^{1/2}, \tag{34}$$

and $\bar{\omega}_i = (\omega_i + \omega_{i+1})/2$ (Holthuijsen, 2007).

2.4. Air turbine

Based on the turbine's rotational speed, $\Omega(t)$, and available pressure head, $p_t(t)$, the instantaneous pressure coefficient are defined as

$$\Psi(t) = \frac{p_t(t)}{\rho_{\mathrm{ref}}\Omega^2(t)D^2}, \tag{35}$$

the flow rate coefficient,

$$\Phi(t) = \frac{w_t(t)}{\rho_{\mathrm{ref}}\Omega(t)D^3}, \tag{36}$$

the power (torque) coefficient,

$$\Pi(t) = \frac{T_t(t)}{\rho_{\mathrm{ref}}\Omega(t)^2 D^5}, \tag{37}$$

and the efficiency,

$$\eta_t(t) = \frac{\Pi(t)}{\Phi(t)\Psi(t)}, \tag{38}$$

where $p_t(t)$ is the turbine pressure head ($p_t(t) = p_c(t)$ in the absence of a valve in series with the turbine), $q_t(t) = w_t(t)/\rho_{\mathrm{ref}}$ is the turbine volumetric flow rate, ρ_{ref} is the air density at the turbine entrance (either ρ_a or $\rho_c(t)$ depending on the flow direction through the turbine), D the turbine rotor diameter, and $T_t(t)$ the turbine shaft torque (Dixon and Hall, 2013).

The Wells turbine presents an approximately linear relationship between the turbine pressure coefficient and the turbine flow rate coefficient under free-stall conditions (Carrelhas et al., 2024),

$$\Phi(t) = K_L\Psi(t), \tag{39}$$

giving (see Eq. (10))

$$k_L(t) = \frac{K_L D}{\Omega(t)}. \tag{40}$$

If a Wells turbine is controlled under constant rotational speed, Eq. (10) is approximately satisfied. This does not hold for turbines exhibiting non-linear relationships between mass flow rate and available pressure head (Eq. (26)), as is the case for impulse turbines (Falcão and Henriques, 2019).

This work focuses on a biradial turbine with fixed guide vanes to demonstrate the new tool as an example. The turbine toolbox routine can be easily updated to include the characteristics of other turbine types. Previous work (Carrelhas et al., 2023a) use a high-speed safety valve in series with the turbine. The results of the efficiency, power and pressure coefficient as a function of the flow coefficient for different valve's shutter angular positions u are shown in Fig. 2. The results are used exclusively to demonstrate the application of the proposed tool. Detailed analysis of these results is presented in Carrelhas et al. (2023a).

Table 1
Variation of the head loss coefficient with the angular position u of the shutter in a flat disc butterfly valve within a duct (Idelchik, 2008).

u [°]	90	80	70	60	50	40	30	20	15	0
$\xi(u)$	0.60	0.85	1.7	4.0	9.4	24	67	215	400	∞

2.5. Control valve

A control valve can be used in OWC systems in series or in parallel with the PTO.

2.5.1. Safety valve in parallel with the turbine

Introducing a valve in parallel with the turbine (bypass valve), the pressure drop in the turbine and the valve are equal to the chamber pressure oscillation, i.e., $p_t(t) = p_{bv}(t) = p_c(t)$. Assuming fully turbulent flow, the mass flow rate through the bypass valve is

$$w_{bv}(t) = \mathrm{sgn}(p_c(t))\left(\frac{2\rho_c(t)|p_c(t)|}{\xi(u)}\right)^{1/2} S_{bv}, \tag{41}$$

where S_{bv} is the valve's fully open passage area and $\xi(u)$ is the head loss coefficient, which is a non-linear function of the valve shutter angular position, u (Idelchik, 2008). As an illustrative example, Table 1 presents the head loss coefficient, $\xi(u)$, for a flat disc butterfly valve installed in a duct, expressed as a function of the shutter opening angle.

2.5.2. Safety valve in series with the turbine

Introducing a valve in series with the turbine, the pressure drop in the turbine is the difference between the chamber pressure oscillation $p_c(t)$ and the valve pressure drop $p_{sv}(t)$,

$$p_t(t) = p_c(t) - p_{sv}(t). \tag{42}$$

Assuming fully turbulent flow, the valve's pressure drop can be related to the turbine flow rate $q_t(t)$ as

$$p_{sv}(t) = \mathrm{sgn}(p_c(t))\xi(u)\frac{\rho_{\mathrm{ref}}}{2}\left(\frac{q_t(t)}{S_{sv}}\right)^2, \tag{43}$$

where S_{sv} is the valve's fully open passage area, ρ_{ref} the air density at valve's entrance and $\xi(u)$ the head loss coefficient (see Table 1 as an example).

2.6. Electrical generator

This work considers normalised experimental results of a 30 kVA squirrel cage electrical machine grid-connected through a frequency converter, as presented in Carrelhas et al. (2023b). It has two pairs of poles and was tested for rotational speeds between 400 and 2980 r.p.m.. Fig. 3 depicts the efficiency of the generator for a given turbine power, normalised by the generator's rated power and rotational speed. The rational polynomial functions that fit these data points are listed in Carrelhas et al. (2023b) and were used for this work. The electrical generator toolbox routine can be easily updated to include the characteristics of other generator types.

2.7. PTO control

The turbine's rotor is assembled in series with the generator's shaft by couplings. From Newton's second law of motion, the relationship between the produced torque in the turbine, $T_t(t)$, and the generator's counter torque, $T_g(t)$, to attain a given rotational speed is

$$I\frac{\mathrm{d}\Omega(t)}{\mathrm{d}t} = T_t(t) - T_g(t), \tag{44}$$

where I is the sum of inertia of the turbine, generator and coupling rotating masses.

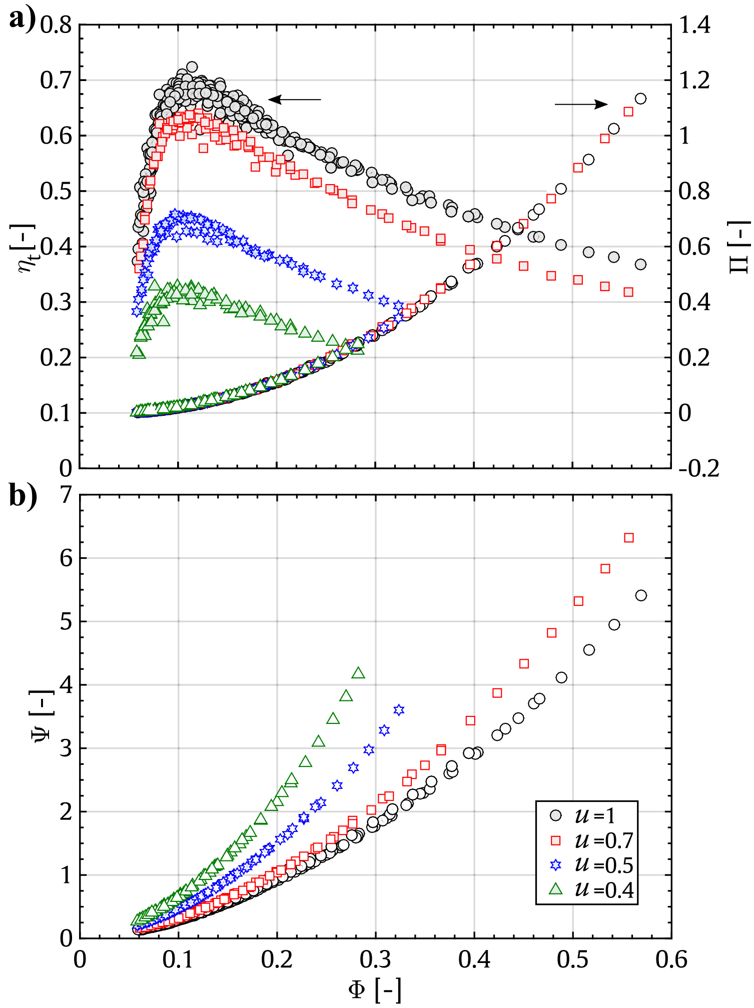

Fig. 2. Biradial turbine characteristics of (a) efficiency and power coefficient and (b) pressure coefficient for different flow coefficients. The results are for inhalation flow and different valve shutter positions, $u = 1$, 0.7, 0.5 and 0.4 (Carrelhas et al., 2023a).

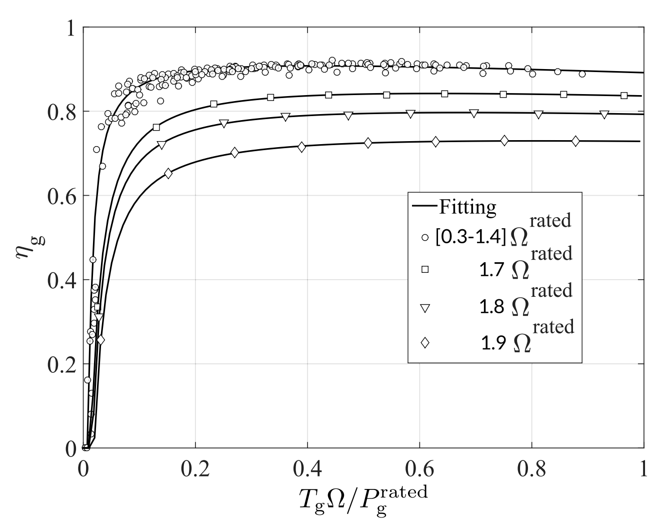

Fig. 3. Efficiency of the generator, η_g, as a function of the turbine power normalised by the generator rated power, $T_g\Omega/P_g^{\text{rated}}$, and the rotational speed, Ω. The value of Ω_{rated} is 1470 r.p.m..
Source: Adapted from Carrelhas et al. (2023b).

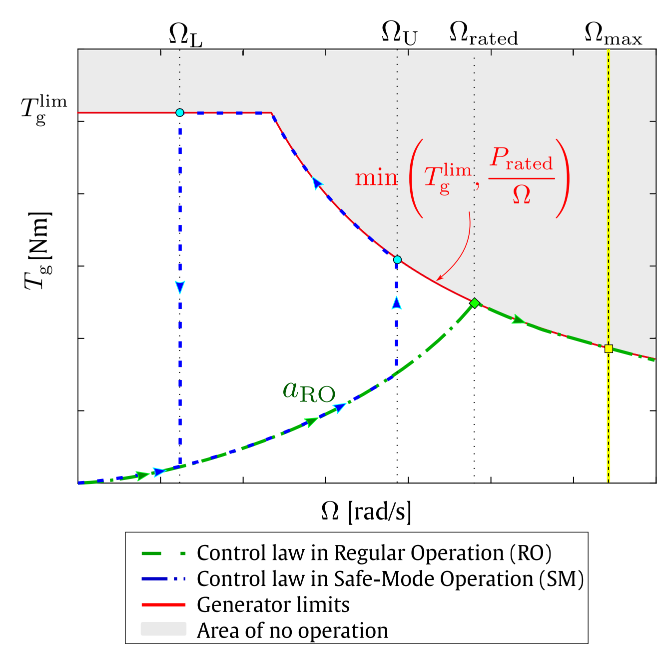

Fig. 4. Generator's counter torque as a function of the turbine rotational speed, Ω, for the two operation modes.

Fig. 4 shows a schematic representation of the control algorithm used in this work. It follows the same strategy as in Carrelhas and Gato (2023). The two modes of operation are: (1) safe mode (SM) in higher energetic sea states, and (2) regular operation mode (RO) in low- and medium-energetic sea states.

For regular operation, the control law

$$T_g^{RO}(t) = \min\left(a_{RO}(\mathrm{rms}(\Omega(t)))\Omega^b(t),\ P_g^{rated}/\Omega(t),\ T_g^{max}\right) \tag{45}$$

is used and follows the green dot-dashed line in Fig. 4. Here the values of a_{RO} and b maximise the generator's electric power output while accounting for the effect of the electric generator's efficiency and the inertia of the rotating masses (Carrelhas and Gato, 2023).

The following triggers the control algorithm to enter SM operation: (1) the average available power, $\bar{P}_a(t)$, for a given time range, Δt_{CL}, surpasses a threshold value, P_{thrs}, and (2) the rotational speed for a given time step surpasses a threshold value, Ω_U. The mean available pneumatic power is,

$$\bar{P}_a(t) = \frac{1}{\Delta t_{CL}} \int_{t-\Delta t_{CL}}^{t} q_t(t) p_c(t) \mathrm{d}t\,. \tag{46}$$

The control law is then

$$T_g^{SM}(t) = T_g^{max}(\Omega(t)) = \min\left(P_g^{rated}/\Omega(t), T_g^{lim}\right)\,. \tag{47}$$

The electric generator's maximum permitted electromagnetic torque is represented by Eq. (47). The control law is presented in a blue dot-dashed line in Fig. 4.

When the instantaneous rotational speed falls below a lower threshold, Ω_L, and the mean available pneumatic power, $\bar{P}_a(t)$, during a given time interval, Δt_{CL}, falls below P_{thrs}, the control algorithm shifts to RO.

The safety valve is actuated for partial closure (SMV) whenever the available energy is excessive for the SM operation. This is triggered when: (1) the average available power, $\bar{P}_a(t)$, for a given time range, Δt_{CL}, surpasses a threshold value, P_{thrsV}, and (2) the rotational speed for a given time step surpasses a threshold value, Ω_{UV}.

The control algorithm goes into SMV operation when:

1. the mean available pneumatic power, $\bar{P}_a(t)$, during a given time interval, Δt_{CLV}, is larger than a given threshold value P_{thrsV} and;
2. the instantaneous rotational speed is larger than a given upper-threshold value, $\Omega(t) > \Omega_{UV}$.

3. WEC-sim simulink OWC model files

Fig. 5 illustrates the primary Simulink block diagram to study a fixed OWC with WEC-SIM: (1) Rigid Body, (2) Translational Constraint and (3) Global Reference Frame. The piston is represented by the Rigid Body block. This block is responsible for using the hydrodynamic and wave data to calculate all the forces acting on the body and solve for the corresponding motion (National Renewable Energy Laboratory and Sandia National Laboratories, 2022). It is ready to solve Eq. (1), where all the calculated forces converge to a summation block, except for the pressure force on the piston, $f_p(t)$. The proposed new Simulink block, hereinafter called Pressure Function block, makes use of the displacement and velocity of the piston (rigid body) inside the Rigid Block for the calculation of the piston force $f_p(t)$. Subsequently, it adds it to the total force summation bus.

What follows allows for integration of any type of: (1) turbine, (2) generator, (3) PTO control and (4) use of series and/or parallel valve. The Pressure Function block has as inputs and output the variables listed in Table 2. The pseudocode of this block is listed below. As a result, the output is the pressure force on the piston $f_p(t)$ which is later used for the solution of Eq. (1).

1. **Air turbine and series valve:** Calculate the mass flow rate of the turbine, $w_t(t)$, given by Eq. (26) from the turbine characteristic curve fittings for $\Phi(\Psi, u)$ and the turbine shaft torque $T_t(t)$ from $\Pi(\Phi)$ for a given valve's shutter position (see Eqs. (35) to (37)).

Table 2
Pressure force Simulink block: Inputs and outputs.

Inputs, time step t	Outputs, time $t+\Delta t$
Piston displacement	Piston pressure force
Piston velocity	
Chamber pressure	Chamber pressure
Rotational speed	Rotational speed
Valve position	Valve position

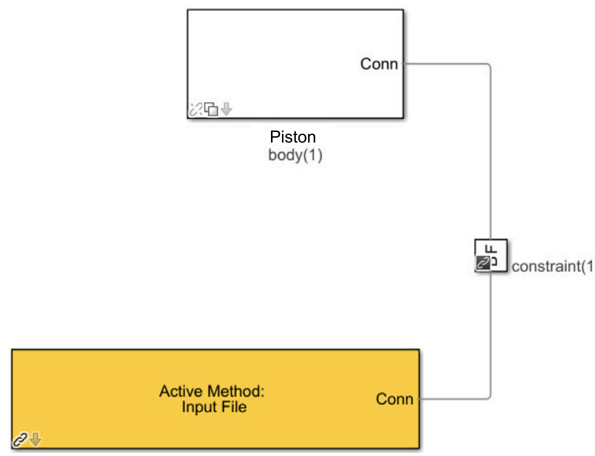

Fig. 5. New Simulink model blocks to simulate a fixed-structure OWC WEC with WEC-Sim.

Table 3
OWC chamber dimensions (see Fig. 6). The chamber width is L.

b_1	3.09 m
h	5.65 m
l_0	6.70 m
h_1	2.85 m
t_1	6.65 m
L	4.50 m

2. **Control of the generator:** Calculate the generator's counter torque $T_g(t)$ to be applied depending on the control strategy. For the test case of this paper, the strategy is as detailed in Section 2.7.
3. **Rotational speed of next time step:** Calculate the rotational speed of the next time step, $\Omega(t + \Delta t)$ using Eq. (44).
4. **Electrical power:** The electrical power output $P_g(t)$ is calculated from efficiency maps of the generator. The inputs are the generator's counter torque, $T_g(t)$, and the rotational speed, $\Omega(t)$.
5. **Safety valve in parallel with the turbine:** The mass flow rate that passes by the bypass valve is computed using Eq. (41) with the pressure oscillation $p_c(t)$ and the valve's head loss curve fitting as a function of the shutter position $u(t)$. The mass flow rate is zero if there is no parallel valve.
6. **Pressure of the next time step:** Eq. (25) is solved to determine the time derivative of the chamber pressure $\mathrm{d}p_c(t)/\mathrm{d}t$ and by consequence $p_c(t + \Delta t)$.
7. **Pressure force on the piston:** The piston pressure force is calculated by Eq. (27).

4. Fixed-structure OWC test case

The test case is a L-shaped OWC WEC integrated into a breakwater caisson, Fig. 6. The main OWC chamber dimensions are presented in Table 3.

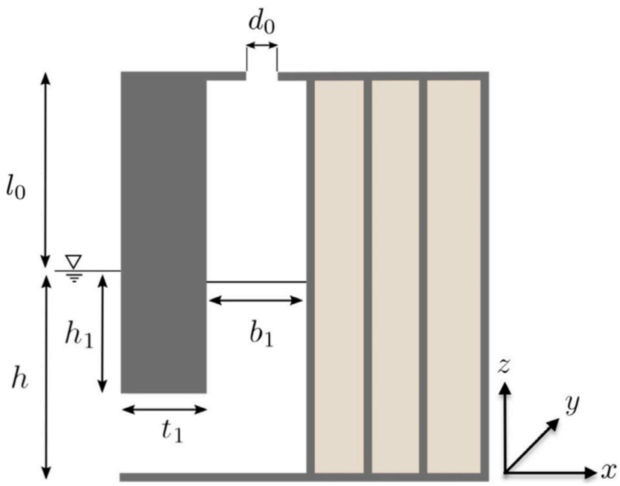

Fig. 6. Cut-section view of the L-shaped OWC integrated into a caisson breakwater (not to scale).
Source: Adapted from Fox et al. (2021).

The hydrodynamic coefficients input to the numerical model described in Section 2 were computed using the WAMIT BEM code (Lee and Newman, 2021). The higher order discretisation method (Lee and Newman, 2021) was applied to discretise the submerged structure, and the free-surface elevation inside the chamber was modelled as a weightless piston. The breakwater was simulated by incorporating vertical walls on both sides of the converter, extending perpendicularly to the wave direction, Fig. 6.

The hydrodynamic coefficients added mass $A(\omega)$, radiation damping $B(\omega)$, and excitation force complex amplitude per unit of wave amplitude $\Gamma(\omega) = F_e/A_w$, of the L-shaped OWC WEC, integrated into a breakwater caisson are represented in a dimensionless form as

$$A^*(\omega^*) = \frac{A(\omega^*)}{\rho_w b_1^3}, \tag{48}$$

$$B^*(\omega^*) = \frac{B(\omega^*)}{\rho_w g^{1/2} b_1^{5/2}}, \tag{49}$$

$$\Gamma^*(\omega^*) = \frac{|\Gamma(\omega^*)|}{\rho_w g b_1^2}, \tag{50}$$

where b_1 is the converter length, ρ_w the water density, g the gravity acceleration, and

$$\omega^* = \omega\sqrt{\frac{b_1}{g}}. \tag{51}$$

The vertical walls, on each side of the converter, used to simulate the breakwater effect have 60 m length. The coefficients computed for the mean water level $h = 5.65$ m (Fig. 6) are plotted in Fig. 7.

5. Results

This Section summarises frequency-domain and time-domain results, considering regular and irregular waves, linear and non-linear turbines, air chamber compressibility, the safety valve and turbine generator control.

For simplicity, the expansion and compression of the air inside the OWC pneumatic chamber are assumed isentropic ($n = \gamma$), constituting a reasonable assumption for the present calculations (Falcão and Henriques, 2019).

The aim is to validate the new Simulink WEC-Sim model by cross-checking it with an in-house code and to develop a standard, reproducible benchmarking procedure for numerically simulating fixed OWC WECs. The uncertainty associated with the new Simulink model

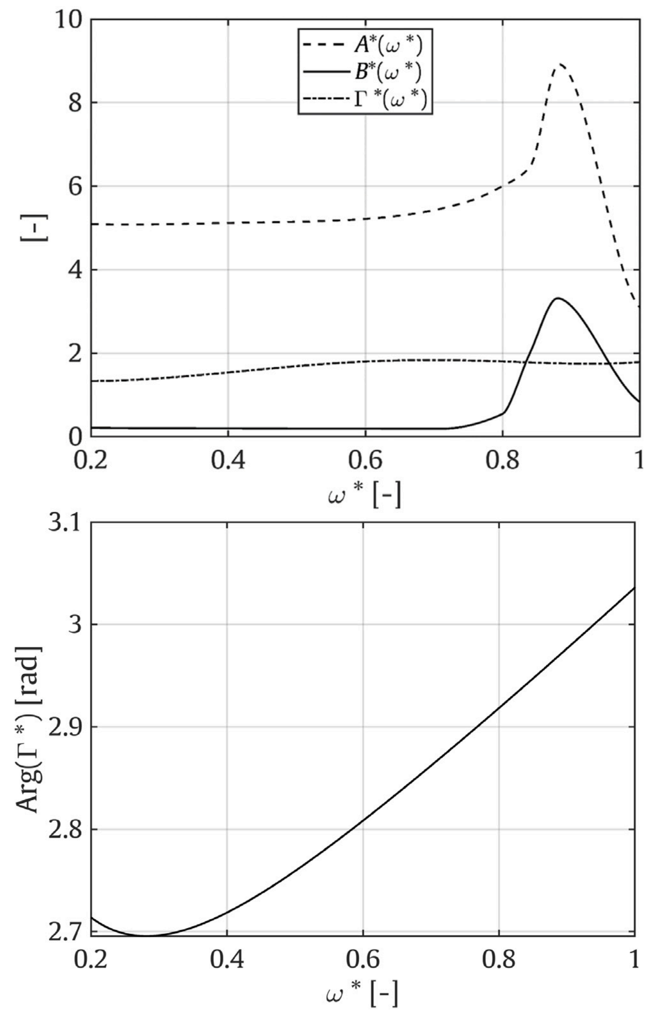

Fig. 7. Dimensionless hydrodynamic coefficients A^*, B^*, Γ^* and the excitation force complex amplitude phase as a function of the normalised frequency ω^*, for L-shaped OWC WEC integrated into a breakwater caisson.

blocks for simulating OWC WECs is illustrated in the following Sections. Section 5.1 discusses the model's performance for regular waves using a linear approach. In Section 5.2, the added mass at infinite frequency is analysed. Section 5.3 presents the decay test, which considers three initial disturbances, while Section 5.4 compares the results from WEC-Sim with frequency domain solutions. Section 5.5 provides the results of the OWC non-linear model for regular waves, evaluating the effects of air chamber compressibility, the non-linear turbine, and the safety valve arranged in series and parallel with the turbine. Finally, Section 5.6 demonstrates the practical capabilities of the WEC-Sim OWC module.

5.1. Regular waves linear model

Regular waves and the OWC linear model described in Section 2.2 were considered to assess the time step, the convolution integration time used in the WEC-Sim calculations and the resonance frequency.

Considering a linear turbine with $K_L = 0.0025$ ms, solution of Eqs. (22), (17) and (23) gives the frequency-domain results depicted in Fig. 8, for the dimensionless pressure oscillation amplitude,

$$\mathcal{P}^* = \frac{|\mathcal{P}|}{\rho_w g A_w}, \tag{52}$$

and the capture width ratio, defined as the ratio between the time-averaged power available to the turbine and the time-averaged power

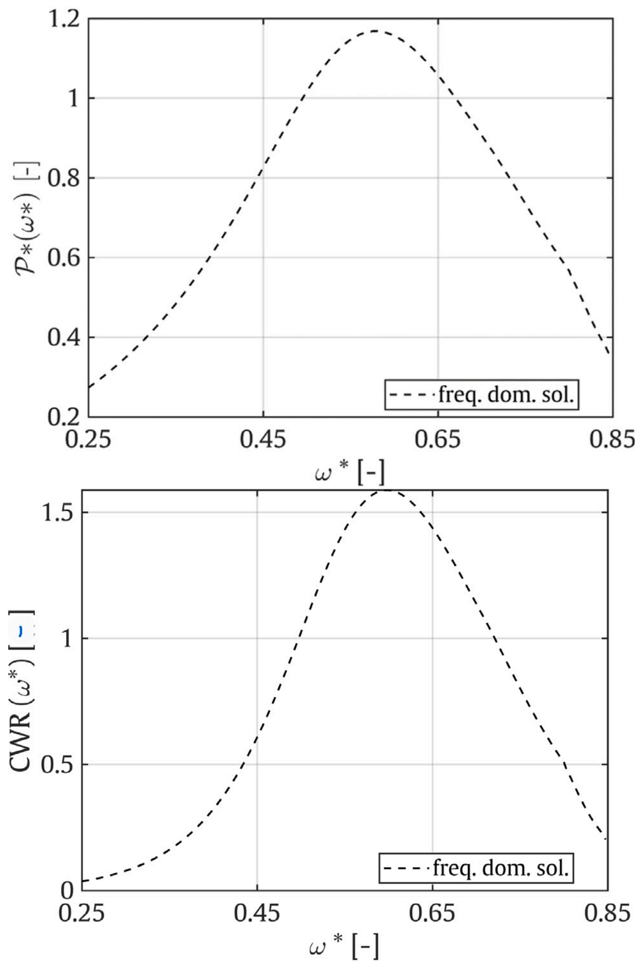

Fig. 8. Frequency domain analytical solution for the pressure amplitude $\mathcal{P}^*$, and capture width ratio, CWR, as a function of the normalised wave frequency, ω^*, for a linear turbine with $k_L = 0.0025$ ms.

transported by a wave with a crest length equal to the converter's width L,

$$\mathrm{CWR} = \frac{\bar{P}_t}{\bar{P}_w L}. \quad (53)$$

5.1.1. Time step

The linear model described in Section 2.2 was implemented for a WEC-Sim time-domain simulation assuming regular waves, setting the regular class wave type, which is appropriate for the solution of an entirely linear model, thus avoiding the calculation of the convolution integral (National Renewable Energy Laboratory and Sandia National Laboratories, 2022).

Low time-discretisation errors require the time step to be much smaller than the wave period under consideration. Typical variance density spectra of Atlantic ocean waves surface elevation are distributed mainly over frequencies $0.3 \leq \omega \leq 1.6$ rad/s corresponding to regular wave periods $4\,\mathrm{s} \leq T \leq 20\,\mathrm{s}$. Wave periods in the range $4.49\,\mathrm{s} \leq T \leq 15.71\,\mathrm{s}$ were selected to run WEC-Sim simulations assuming different time-step values with a ramp time of $2T$ (National Renewable Energy Laboratory and Sandia National Laboratories, 2022). Periodic solutions were observed for $t \geq 10T$. The amplitudes were obtained by taking the mean value of the peaks of the WEC-Sim solutions in the stable range $10T \leq t \leq 20T$.

Fig. 9 depicts the ratio between the free-surface amplitude calculated from the WEC-Sim's periodic solution and the analytical solution

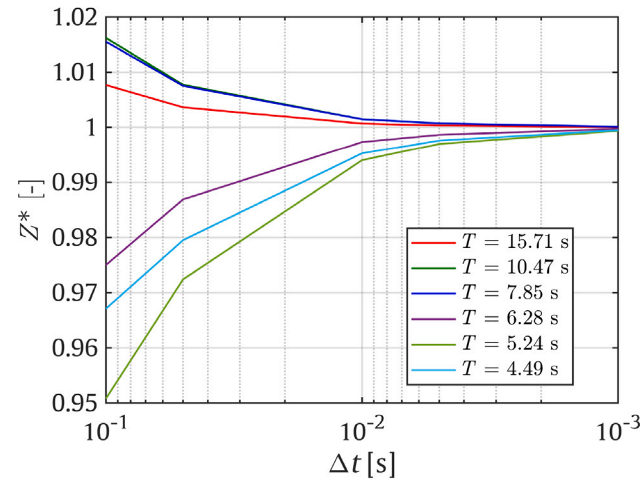

Fig. 9. Ratio between the free-surface amplitude calculated from the WEC-Sim's periodic solution and the analytical solution $Z^*(\omega^*)$ as a function of the WEC-Sim's simulation time step Δt, for several regular waves periods T.

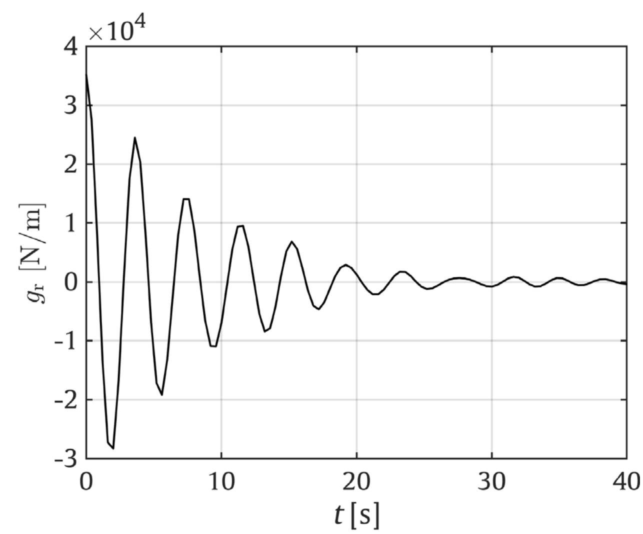

Fig. 10. Function $g_r(t)$ of the radiation force term (Eq. (30)).

$Z^*(\omega^*) = Z_{\mathrm{Sim}}(\omega^*)/Z(\omega^*)$ as a function of the WEC-Sim's simulation time step Δt, for six regular waves periods T. The results show minor time-discretisation errors for time step $\Delta t < 0.01$ s.

5.1.2. Convolution integration time

The linear model described in Section 2.2 was implemented for a time-domain WEC-Sim simulation assuming the regularCIC wave class (National Renewable Energy Laboratory and Sandia National Laboratories, 2022). The difference to the previous calculation is that the radiation forces are calculated using the convolution integral and the infinite frequency added mass (National Renewable Energy Laboratory and Sandia National Laboratories, 2022) to take into account the memory effect in a non-linear time domain calculation.

The convolution integral in Eq. (31) includes the memory function $g_r(t)$ of the radiation force term (Eq. (30)), Fig. 10. Since $g_r(t)$ is of the order $\mathcal{O}(1/t)$ as $t \to \infty$ (Falcão and Justino, 1999), the convolution integral in Eq. (31) is truncated to save computational time for $t < t - \Delta t_{\mathrm{CIC}}$, where t is the present time.

A set of convolution integration time intervals in the range $\Delta t_{\mathrm{CIC}} =$ 20 to 45 s was tested for regular wave frequencies in the range $0.67 \geq \omega^* \geq 0.56$ to identify its influence on the numerical results. Results of

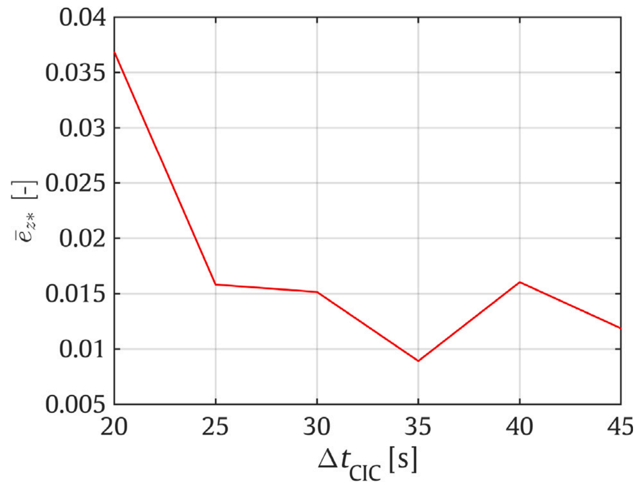

Fig. 11. Average error between the free-surface amplitude calculated from the WEC-Sim's periodic solution, $Z_{\mathrm{Sim}}(\omega^*)$ and the analytical solution, $Z(\omega^*)$, as a function of the WEC-Sim's simulation convolution integral time range, Δt_{CIC}, with time step $\Delta t = 0.01$ s, in the range $0.67 \geq \omega^* \geq 0.56$.

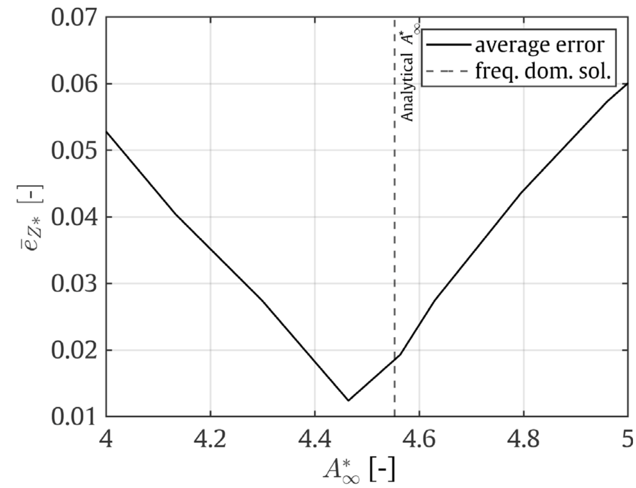

Fig. 12. Average error of the piston displacement amplitude as a function of the normalised added mass at infinity frequency values, in the range $0.67 \geq \omega^* \geq 0.56$.

the average error between the free-surface amplitude calculated from the WEC-Sim's periodic solution, $Z_{\mathrm{Sim}}(\omega^*)$, and the analytical solution, $Z(\omega^*)$, plotted in Fig. 11 as a function of the WEC-Sim's simulation convolution integral time range, Δt_{CIC}, with time step $\Delta t = 0.01$ s, show that setting $\Delta t_{\mathrm{CIC}} = 45$ s gives a favourable balance between accuracy and computational time in the present case. In the remaining of the paper, the convolution integral time interval and the time step are set to $\Delta t_{\mathrm{CIC}} = 45$ s and $\Delta t = 0.01$ s, respectively.

5.2. Added mass at infinity frequency

The solution of Eq. (31) requires accurate calculation of the added mass at infinity frequency, which depends on the OWC geometry.

Using Ogilvie's formulae (Ogilvie, 1964), it is

$$\omega(A(\omega) - A(\infty)) = \int_0^\infty g_{\mathrm{r}}(s)\sin(\omega s)\mathrm{d}s\,. \tag{54}$$

Slight differences in the value of $A(\infty)$ are observed dependent on the selected frequency ω when calculating $A(\infty)$ with Eq. (54) due to numerical errors. To reduce numerical inaccuracies, one option is computing Eq. (54) for a set of frequencies in a representative range and taking the average value. WEC-Sim software gives for the present OWC geometry $A^*(\infty) = 4.563$ which closely approximates the analytical $A^*(\infty)$ as given by Eq. (54), taking the average value for a set of values in the range $0.3 \leq \omega \leq 1.6$ rad/s. It is of interest to verify if using this value produces significant differences compared with the frequency domain solution.

Several values of the added mass at infinity frequency in the range $4 \leq A^*(\infty) \leq 5$ were considered. Each $A^*(\infty)$ value was tested for the set of regular wave periods T = 4.49, 5.24, 6.28, 7.85, 10.47 and 15.71 s and calculating the average error of the piston displacement amplitude depending on the $A^*(\infty)$ value. Results are plotted in Fig. 12. As expected the numerical results become inaccurate when $A^*(\infty)$ deviates significantly from the analytical value. The smallest average error occurs for $A^*(\infty) = 4.464$ which is almost the analytical solution, meaning that the WEC-Sim calculation of the $A^*(\infty)$ is correct and will be adopted in the remaining of the work.

5.3. Decay test

Decay tests were carried out to determine the natural period of OWC heave oscillation, assuming the air chamber open to the atmosphere or the air chamber connected to the atmosphere by a linear turbine. The computation assumes setting the air chamber pressure relative to the atmosphere at $p_{\mathrm{c}}(t) = \rho_{\mathrm{w}} g z(0)$ for $t \leq 0$ in the absence of incident waves. Eq. (31) is then solved taking $f_{\mathrm{e}}(t) = 0$, setting the convolution integral time interval $\Delta t_{\mathrm{CIC}} = 45$ s, time step $\Delta t = 0.01$ s and $A^*(\infty) = 4.563$. In the case of the air chamber open to the atmosphere, it is $p_{\mathrm{c}}(t) = 0$ for $t > 0$. Results plotted in Fig. 13 show that the turbine introduces a large damping in the decay test compared to the open chamber case and that the resonance frequency is $\omega^* = 0.56$ which is in agreement with the analytical solution depicted in Fig. 8. Moreover, the normalised displacement time series depicted in Fig. 13 do not present visible differences for the initial disturbances considered.

5.4. WEC-Sim and the frequency domain solutions comparison

To confirm that the WEC-Sim parameters were carefully tuned, WEC-Sim results for a regular wave small amplitude $A_{\mathrm{w}} = 0.25$ m were obtained assuming the WEC chamber height $l_0 = 6.7$ m and a linear turbine with $k_{\mathrm{L}} = 0.0025$ ms. The numerical results for the piston heave-motion amplitude, defined in a non-dimensional form as

$$\mathrm{RAO} = \frac{|Z|}{A_{\mathrm{w}}}, \tag{55}$$

are displayed in Fig. 14 together with the linear frequency domain solution. Results show that the linear model can provide a good approximation for the WEC subject to small wave amplitude. Non-linear effects become significant in tall pneumatic chambers as will be observed in Section 5.5.1.

5.5. Regular waves non-linear model

Regular waves and the OWC non-linear model described in Section 2.3 were considered to evaluate the effects of the air chamber compressibility, the non-linear turbine and the safety valve in series and parallel with the turbine.

5.5.1. Air chamber compressibility

WEC-Sim was used to assess the air chamber compressibility effect for different values of air chamber heights, considering regular waves, a linear turbine with $k_{\mathrm{L}} = 0.0025$ ms and the OWC non-linear model described in Section 2.3. Results are depicted in Fig. 15 for air chamber heights $l_0 = 6.7, 10, 15$ and 20 m. It is observed that the air chamber compressibility effect can increase or decrease the energy extraction

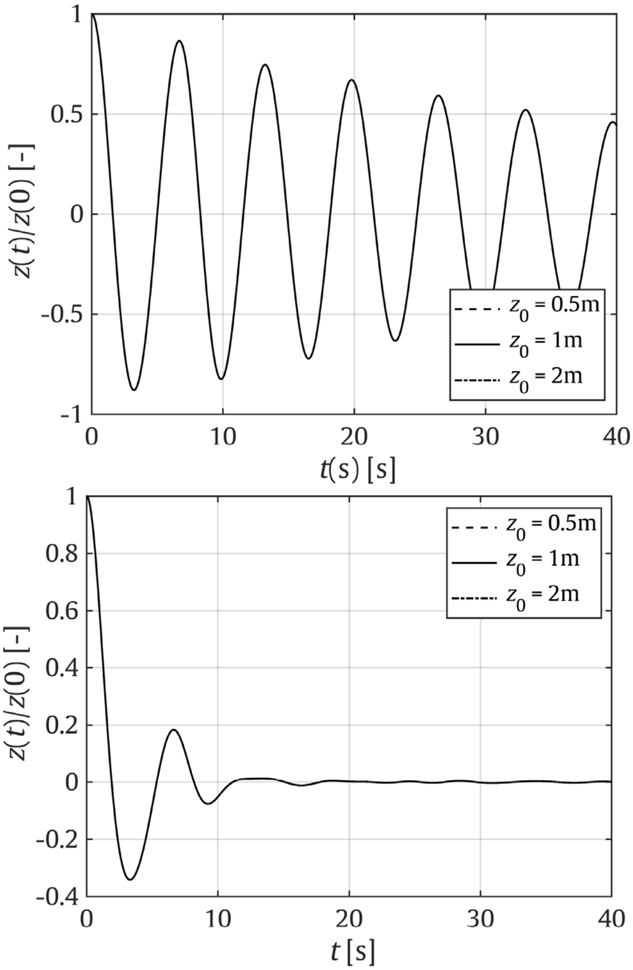

Fig. 13. Time series of the heave decay test WEC-Sim's solution $z^*(t) = z(t)/z(0)$, for three initial displacements, assuming $\Delta t_{\mathrm{CIC}} = 45\,\mathrm{s}$ with time step $\Delta t = 0.01\,\mathrm{s}$: (a) Air chamber open to the atmosphere, (b) air chamber with a $k_{\mathrm{L}} = 0.0025\,\mathrm{ms}$ linear turbine.

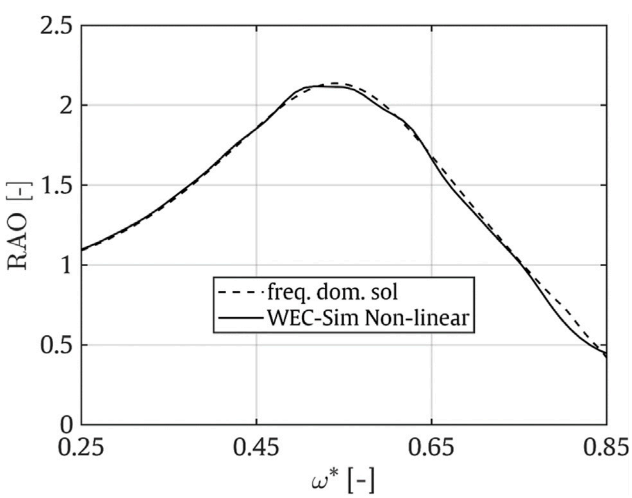

Fig. 14. Frequency domain and WEC-Sim solutions comparison for the normalised internal free-surface amplitude, RAO, as a function of the normalised wave frequency, ω^*, considering a small amplitude regular wave $A_{\mathrm{w}} = 0.25\,\mathrm{m}$, a linear turbine with $k_{\mathrm{L}} = 0.0025\,\mathrm{ms}$, and chamber height $l_0 = 6.7\,\mathrm{m}$.

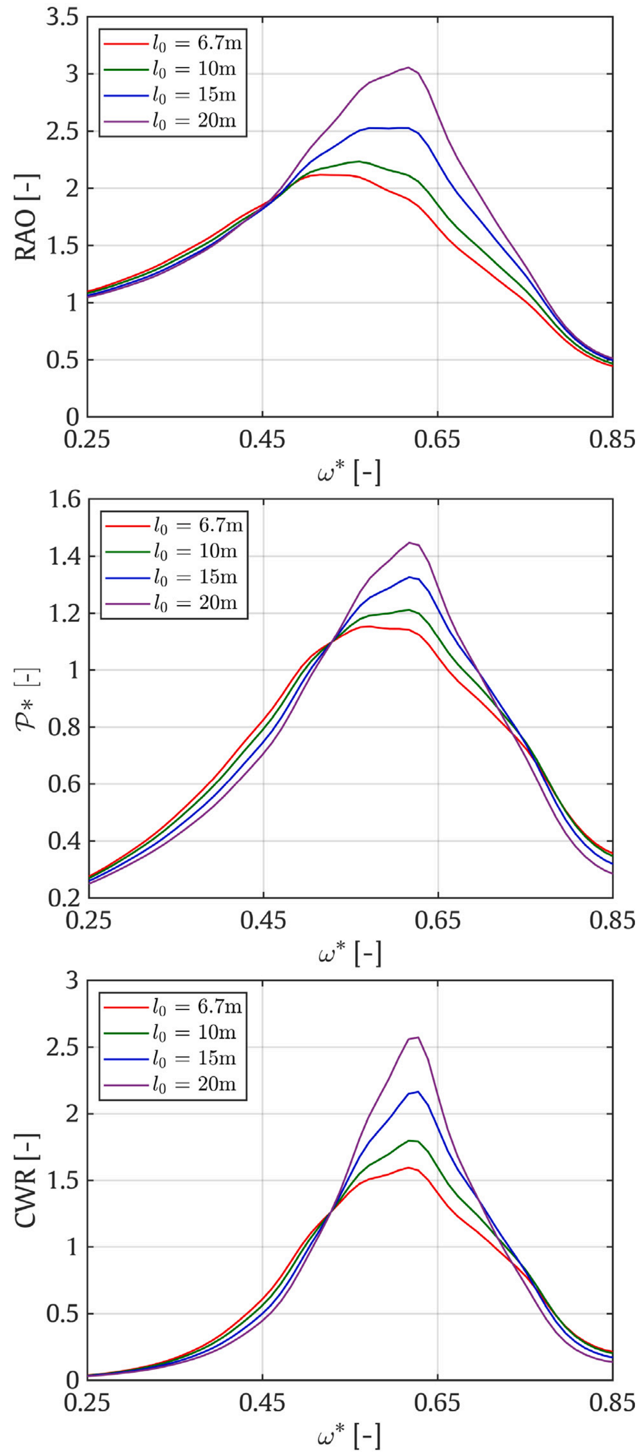

Fig. 15. Numerical solution for the normalised internal free-surface amplitude, RAO, pressure amplitude $\mathcal{P}^*$, and capture width ratio, CWR, as a function of the normalised wave frequency, ω^*, considering regular waves, a linear turbine with $k_{\mathrm{L}} = 0.0025\,\mathrm{ms}$ and the OWC non-linear model, for four air chamber heights l_0.

depending on the regular-wave frequency, as reported in Falcão et al. (2022). There is a frequency value – named Equicompressum Nullum – for which the air chamber compressibility does not affect the pressure (Portillo et al., 2023) while the normalised free-surface amplitude still depends on the air chamber height. The Equicompressum Nullum frequency can be calculated from Eq. (17) giving $\omega^* = 0.524$, which is in agreement with the results plotted in Fig. 15.

It is observed that the non-linear effect introduced by the air chamber compressibility slight changes the normalised periodic solution, giving a slight increase (decrease) in the normalised pressure peaks (troughs) with the regular wave amplitude increase.

5.5.2. Non-linear turbine

Under free-stall conditions, Eq. (10) approximates the mass flow rate of a Wells turbine as a function of the available pressure head, at constant rotational speed (Carrelhas et al., 2024). Other types of self-rectifying turbines, such as the biradial turbine (Carrelhas et al., 2019) present a non-linear relationship between the mass flow rate and available pressure head (Eq. (26)) which is approximately given by

$$\Phi(t) = \mathrm{sgn}(\Psi(t))K_{\mathrm{N}}|\Psi(t)|^{\frac{1}{2}}\,, \tag{56}$$

where K_{N} is a dimensionless constant, depending on the turbine geometry, giving

$$w_{\mathrm{t}}(t) = \mathrm{sgn}(p_{\mathrm{c}}(t))k_{\mathrm{N}}|p_{\mathrm{c}}(t)|^{1/2}\,, \tag{57}$$

where

$$k_{\mathrm{N}} = \rho_{\mathrm{ref}}^{1/2}D^2K_{\mathrm{N}}\,, \tag{58}$$

showing that the mass flow rate through the biradial turbine depends on the turbine size and geometry but it is approximately independent of the rotational speed.

Following the linearisation method for regular waves presented in Refs. (Oikonomou et al., 2021; Fox et al., 2021), the time-average power available to the linear and non-linear turbines are equal if the turbines coefficients are related as

$$k_{\mathrm{L}} = \frac{3\pi}{8}k_{\mathrm{N}}\mathcal{P}^{-1/2}\,, \tag{59}$$

which depends on the amplitude of the pressure oscillation, $\mathcal{P}$. The relation between the pressure amplitude of the linear turbine, $\mathcal{P}$, and the wave amplitude, A_{w}, is frequency dependent (Fig. 8). Table 4 present the values of the non-linear turbine coefficient k_{N} correspondent to the linear turbine coefficient $k_{\mathrm{L}} = 0.0025$ ms, for regular wave amplitudes in the range $0.1\,\mathrm{m} \geq A_{\mathrm{w}} \geq 1.5\,\mathrm{m}$ and wave frequencies $\omega = 1.0$ and 0.6 rad/s.

Calculations were performed to compare the effect of the turbine's non-linear and linear characteristics on the available pneumatic power to the turbine. As expected, results shown in Table 4 indicate that the non-linear turbine provides a similar available power to the turbine for the design wave amplitude as the linear turbine. For constant non-linear turbine coefficients k_{N} and $\omega = 1.0$ rad/s, less available power is obtained as the regular wave amplitude increases. In contrast, higher available power is obtained for constant wave amplitude as k_{N} increases. Different behaviour is observed for $\omega = 0.6$ rad/s, indicating that specific comparison between a linear and a non-linear turbine damping must consider a complete wave climate, as it influences the OWC hydrodynamic response.

5.5.3. Series or parallel safety valve with the turbine

The use of a safety valve in series (throttling) or parallel (bypass) with the turbine was assessed considering regular waves with $A_{\mathrm{w}} = 1.5$ m and $\omega = 1.0$ rad/s, a non-linear turbine with $k_{\mathrm{N}} = 0.2695\,\mathrm{kg}^{1/2}\mathrm{m}^{1/2}$, a plane disc butterfly valve (see Section 2.5), and the OWC non-linear model described in Section 2.3. Without the series or parallel safety valves, results in Table 4 show CWR $= 1.489$.

Table 4
Capture width ratio for non-linear and linear turbines. The non-linear turbine coefficients k_{N} correspond to the linear turbine coefficient $k_{\mathrm{L}} = 0.0025$ ms, for regular wave amplitudes in the range $0.1\,\mathrm{m} \geq A_{\mathrm{w}} \geq 1.5\,\mathrm{m}$ and wave frequency $\omega = 1.0$ and 0.6 rad/s.

$\omega = 1.0$ rad/s					
A_{w} [m]	non-linear turbine k_{N} [kg$^{1/2}$m$^{1/2}$]				linear turbine k_{L} [ms]
	0.0760	0.1700	0.2420	0.2950	0.0025
0.1	1.484	2.481	2.685	2.627	1.475
0.5	0.734	1.485	1.950	2.160	1.473
1.0	0.531	1.111	1.493	1.740	1.479
1.5	0.439	0.929	1.279	1.489	1.473
$\omega = 0.6$ rad/s					
A_{w} [m]	non-linear turbine k_{N} [kg$^{1/2}$m$^{1/2}$]				linear turbine k_{L} [ms]
	0.0475	0.0996	0.1500	0.1850	0.0025
0.1	0.136	0.057	0.027	0.018	0.136
0.5	0.114	0.136	0.103	0.078	0.136
1.0	0.088	0.138	0.136	0.119	0.136
1.5	0.074	0.127	0.142	0.136	0.136

Table 5
Capture width ratio as a function of the bypass valve shutter position u for regular waves with $A_{\mathrm{w}} = 1.5$ m and $\omega = 1.0$ rad/s, and a non-linear turbine with $k_{\mathrm{N}} = 0.2695\,\mathrm{kg}^{1/2}\mathrm{m}^{1/2}$, as given by the OWC non-linear model.

u [°]	90	40	33.8	33.2	30
$\xi(u)$	0.6	24	45	48	67
CWR	1.49	1.31	1.28	1.27	1.19

Table 6
Standard deviation of the wave elevation σ_ζ, internal free-surface elevation σ_z, chamber pressure $\sigma_{p_{\mathrm{c}}}$, normalised chamber pressure $\sigma^*_{p_{\mathrm{c}}} = \sigma_{p_{\mathrm{c}}}/(\rho_{\mathrm{w}}g\sigma_\zeta)$ and capture width ratio CWR.

H_{s} [m]	T_{e} [s]	σ_ζ [m]	σ_z [m]	$\sigma_{p_{\mathrm{c}}}$ [Pa]	$\sigma^*_{p_{\mathrm{c}}}$ [–]	CWR [–]
1.7	10.8	0.44	0.64	2498	0.57	0.31
2.7	10.0	0.69	0.93	3369	0.49	0.21
3.8	12.9	1.04	1.30	4261	0.41	0.15

Table 7
Turbine generator control results with bypass valve.

H_{s} [m]	T_{e} [s]	$\bar{P}_{\mathrm{a}}$ [kW]	$\bar{P}_{\mathrm{t}}$ [kW]	$\bar{P}_{\mathrm{g}}$ [kW]	$\bar{\eta}_{\mathrm{t}}$ [–]	$\bar{\eta}_{\mathrm{g}}$ [–]	Bypass valve
2.7	12.0	27.1	15.7	14.0	0.58	0.88	No
4.5	10.5	78.2	29.3	25.5	0.37	0.87	No
4.5	10.5	54.8	27.5	23.0	0.50	0.83	Yes

The bypass valve diameter was set to $D_{\mathrm{bv}} = 1.1$ m. Partially opening the bypass valve is expected to drop the CWR to 1.274, corresponding to $k_{\mathrm{N}} = 0.2220\,\mathrm{kg}^{1/2}\mathrm{m}^{1/2}$ (see Table 4) while keeping the other conditions. Table 5 presents the CWR results for several valves' shutter positions. It is observed that setting the shutter position at an angle of $u = 33.4°$ provides the desired CWR $= 1.274$. The comparison of the chamber pressure, turbine flow rate and available power for the corresponding cases with and without bypass valve are depicted in Fig. 16. Opening the bypass valve relieves pneumatic energy, leading to smaller CWR and chamber overpressure is avoided.

The series valve diameter was set to $D_{\mathrm{bv}} = 0.75$ m and the shutter position was set at $u = 59.9°$ which gives $\xi(u) = 4.3$. The partial closure of the series valve decreases the flow and available power to the turbine. The comparison of the chamber pressure, turbine flow rate and available power for the corresponding cases with and without the series valve are plotted in Fig. 17. In the present case, results in Fig.

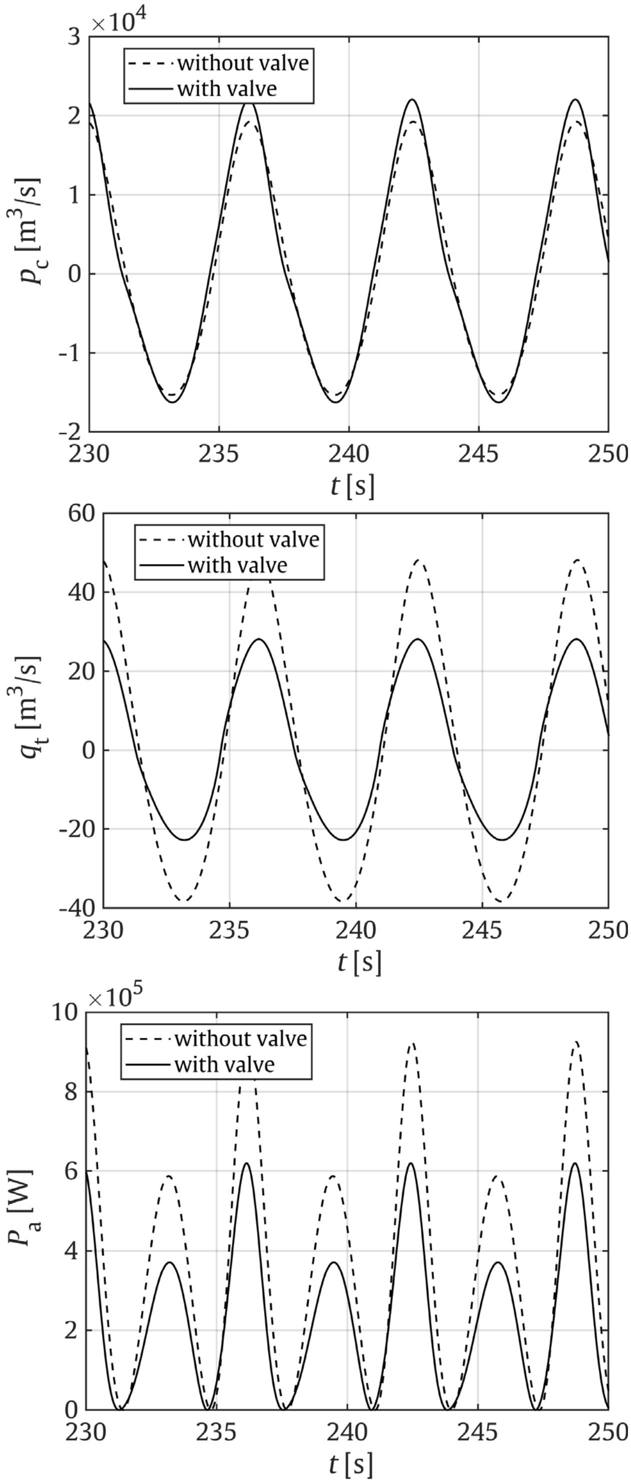

Fig. 16. Numerical solution for the chamber pressure $p_c(t)$, turbine volumetric flow rate $q_t(t)$ and turbine available power $P_a(t)$ for regular waves with A_w = 1.5 m and $\omega = 1.0$ rad/s, a non-linear turbine with $k_N = 0.2695\,\mathrm{kg}^{1/2}\mathrm{m}^{1/2}$, and the OWC non-linear model, with and without plane disc butterfly bypass valve.

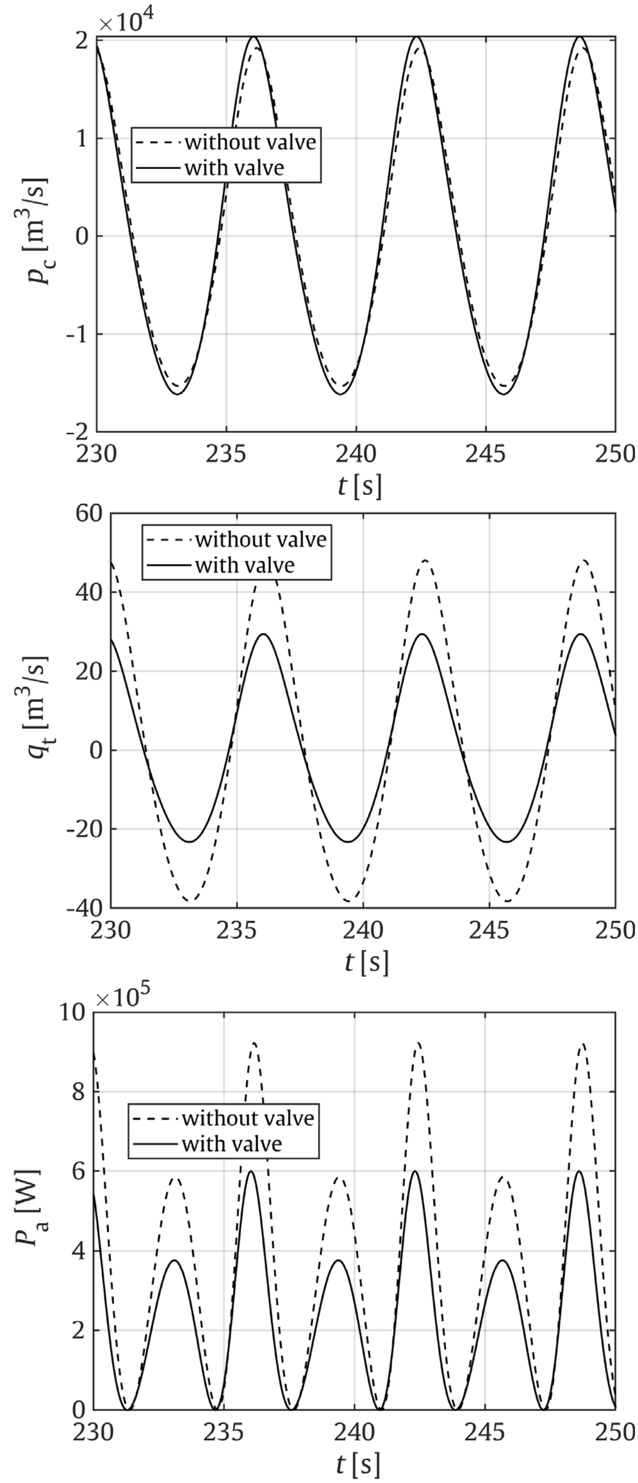

Fig. 17. Numerical solution for the chamber pressure $p_c(t)$, turbine volumetric flow rate $q_t(t)$ and turbine available power $P_a(t)$ for regular waves with A_w = 1.5 m and $\omega = 1.0$ rad/s, a non-linear turbine with $k_N = 0.2695\,\mathrm{kg}^{1/2}\mathrm{m}^{1/2}$, and the OWC non-linear model, with the plane disc butterfly series valve fully open and partially closed.

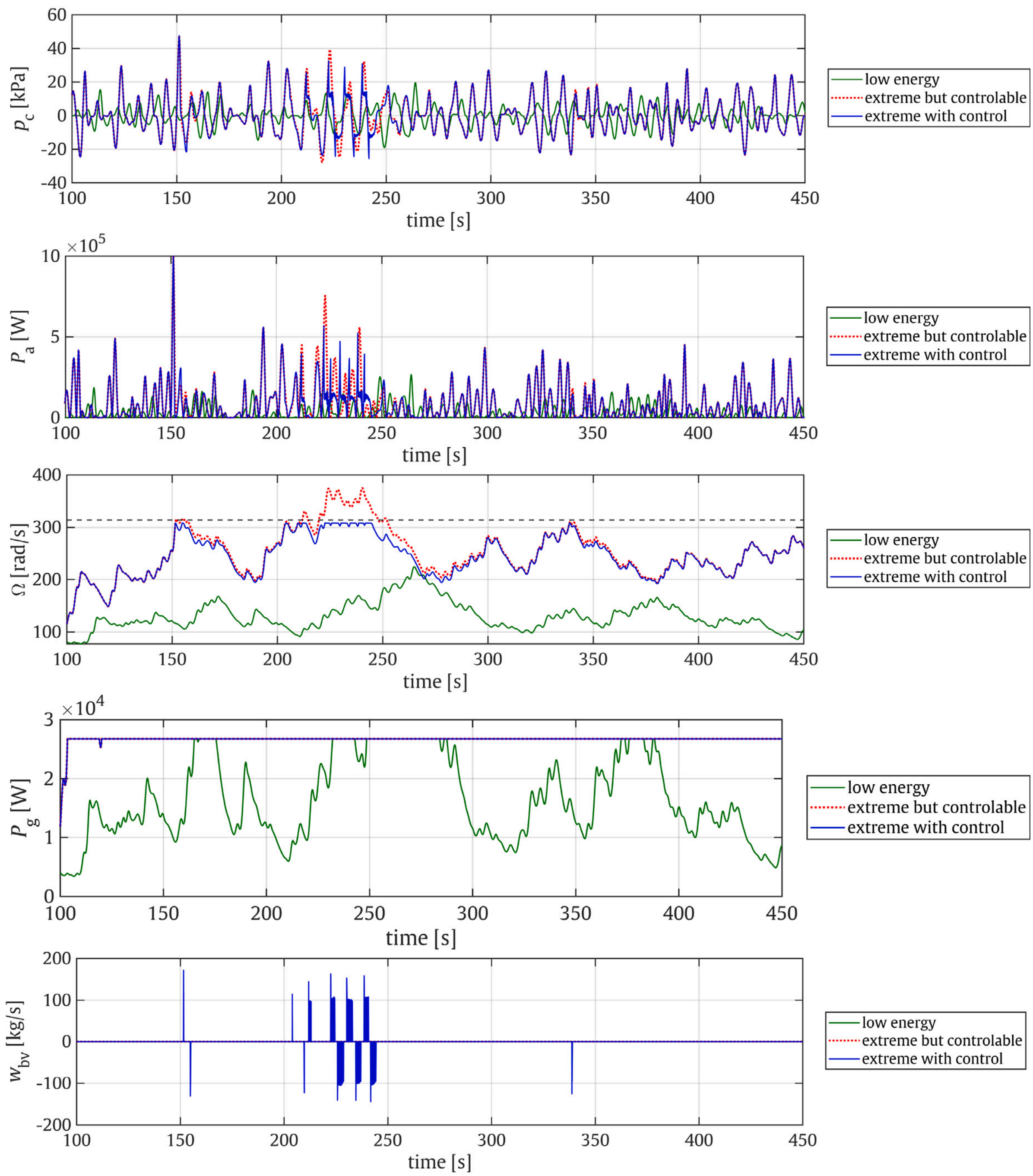

Fig. 18. Chamber pressure $p_c(t)$, turbine available power $P_a(t)$, turbine rotational speed $\Omega(t)$, electrical power output $P_g(t)$ and bypass valve mass flow rate $w_{bv}(t)$ for a biradial turbine with $D = 0.75$ m and two sea states with and without bypass valve operation (see Table 7).

17 reveal that the pressure in the chamber is not significantly affected by the valve's partially closure while the flow and the available power decrease giving CWR $= 0.957$, which corresponds to the operation of a turbine with $k_N = 0.1556\,\mathrm{kg}^{1/2}\mathrm{m}^{1/2}$ with the valve's fully open (see Table 4).

5.6. Irregular waves

5.6.1. Linear turbine

A set of three sea states, with increasing energy, were considered to evaluate the performance of a linear turbine with $k_L = 0.0025$ ms. The numerical results are displayed in Table 6 in terms of the standard deviation of the wave elevation σ_ζ, internal free-surface elevation σ_z, chamber pressure σ_{p_c}, normalised chamber pressure $\sigma^*_{p_c} = \sigma_{p_c}/(\rho g \sigma_\zeta)$ and capture width ratio CWR. The overall dimensional variables increase as the wave power increase whereas the non-dimensional variables $\sigma^*_{p_c}$ and CWR decrease as the sea-state energy period move away from the wave period that gives maximum CWR for regular waves (see Fig. 14).

5.6.2. Turbine generator control with bypass valve

The control strategy of Section 2.7 was applied with a PTO consisting of a $D = 0.75$ m rotor diameter biradial turbine with the performance curves of Fig. 2, the 30 kW electrical generator of Section 2.6 and a bypass butterfly valve with diameter $D_{bv} = 1.1$ m, as described in Section 2.5.1. One sea state with low and other with high energy were considered as presented in Table 7. The high-energy sea state study includes two cases: operation with and without the bypass valve. Simulations run for 30 min. The resulting time series of chamber pressure, $p_c(t)$, turbine available power, $P_a(t)$, turbine rotational speed, $\Omega(t)$, electrical power output, $P_g(t)$, and bypass valve mass flow rate, $w_{bv}(t)$, are depicted in Fig. 18.

Results plotted in Fig. 18 show regular operation with rotational speed within the operational range without using the bypass valve (see green line), giving high turbine and generator average efficiencies, $\bar{\eta}_t = 0.58$ and $\bar{\eta}_g = 0.88$, respectively, for an average turbine available power $\bar{P}_a = 27.1\,\mathrm{kW}$, as presented in Table 7. In the case of the high energy sea state operating without the bypass valve, the average turbine available power is excessive, $\bar{P}_a = 78.2\,\mathrm{kW}$, and the reduction in the turbine efficiency introduced by the controller is not enough to keep the rotation speed within the operational range (see red line and Table 7). By operating the bypass valve, the average turbine available power becomes $\bar{P}_a = 54.8\,\mathrm{kW}$, the turbine average efficiency increases from $\bar{\eta}_t = 0.37$ to 0.50. In contrast, the generator average efficiency slightly decreases from $\bar{\eta}_g = 0.87$ to 0.83, and the PTO can operate within the rotational speed operational range.

6. Conclusions

A significant deficiency exists in publicly accessible, comprehensive implementations for OWCs within WEC-Sim/Simulink that (i) integrate pneumatic chamber thermodynamics (air compressibility) with (ii) air-turbine models, (iii) flow-control valves (configured in series/parallel with the turbine), and (iv) generator efficiency and PTO control, all within a singular, reproducible workflow. Existing literature on OWCs demonstrates that chamber compressibility and PTO (turbine and generator) dynamics are critical for system performance and present significant modelling and validation challenges. Despite this, no open-source WEC-Sim example consolidates all these components and their controls within a single framework. This paper aims to address this gap.

A novel Simulink block describing the thermodynamics of air compressibility within the pneumatic chamber of an oscillating-water-column (OWC) wave energy converter (WEC) and its power take-off system (PTO) was developed to adapt the WEC-Sim tool for calculating OWC-type WECs. The new features include air compressibility in the pneumatic chamber, linear and non-linear turbines, air valves in series and parallel with the turbine, electrical generators, and control of the turbine-generator set.

A pneumatic chamber integrated into a breakwater was selected as a test case to evaluate the accuracy of the numerical method. The WEC-Sim results for regular waves were compared with those from an in-house frequency-domain linear model to assess the time step, the convolution integration time interval, and the added mass at the infinite frequency to be used in WEC-Sim calculations. Non-linear effects, such as the air chamber's compressibility, nonlinear turbines, and safety valves arranged in series and parallel with the turbine, were assessed.

Finally, results for the complete WEC with PTO control, including using a bypass valve, demonstrate the practical capabilities of the new WEC-Sim OWC module for fixed-structure OWC-type WECs.

Future work includes experimental validation and extending the toolbox for calculating floating-type OWC WECs, as well as integrating mooring models into the WEC-Sim tool.

CRediT authorship contribution statement

A.A.D. Carrelhas: Writing – original draft, Visualization, Validation, Supervision, Software, Methodology, Investigation, Formal analysis, Conceptualization. **L.M.C. Gato:** Writing – original draft, Validation, Supervision, Resources, Project administration, Methodology, Funding acquisition, Formal analysis, Conceptualization. **C.G. Cartaxo:** Writing – review & editing, Visualization, Software, Investigation, Data curation.

Declaration of competing interest

The authors declare that they have no known competing financial interests or personal relationships that could have appeared to influence the work reported in this paper.

Acknowledgements

The authors acknowledge Fundação para a Ciência e a Tecnologia (FCT) for its financial support via projects LAETA Base Funding (DOI: 10.54499/UID/50022/2025) and Carbon-free Ports (DOI: 10.54499/2023.16147.ICDT). The first author was supported by FCT researcher grant No. PRT/BD/154809/2023.

References

Ancellin, M., Dias, F., 2019. Capytaine: A Python-based linear potential flow solver. J. Open Source Softw. 4 (36), 1341. http://dx.doi.org/10.21105/joss.01341.

Carrelhas, A.A.D., Gato, L.M.C., 2023. Reliable control of turbine-generator set for oscillating-water-column wave energy converters: Numerical modelling and field data comparison. Energy Convers. Manage. 282, 116811. http://dx.doi.org/10.1016/j.enconman.2023.116811.

Carrelhas, A.A.D., Gato, L.M.C., Henriques, J.C.C., 2023a. Peak shaving control in OWC wave energy converters: From concept to implementation in the Mutriku wave power plant. Renew. Sustain. Energy Rev. 180, 113299. http://dx.doi.org/10.1016/j.rser.2023.113299.

Carrelhas, A.A.D., Gato, L.M.C., Henriques, J.C.C., A.F.O. Falcão, J. Varandas, 2019. Test results of a 30 kW self-rectifying biradial air turbine-generator prototype. Renew. Sustain. Energy Rev. 109, 187–198. http://dx.doi.org/10.1016/j.rser.2019.04.008.

Carrelhas, A.A.D., Gato, L.M.C., Henriques, J.C.C., Marques, G.D., 2023b. Estimation of generator electrical power output and turbine torque in modelling and field testing of OWC wave energy converters. Energy Convers. Manag.: X 19, 100384. http://dx.doi.org/10.1016/j.ecmx.2023.100384.

Carrelhas, A.A.D., Gato, L.M.C., Morais, F.J.F., 2024. Aerodynamic performance and noise emission of different geometries of Wells turbines under design and off-design conditions. Renew. Energy 220, 119622. http://dx.doi.org/10.1016/j.renene.2023.119622.

Cheng, Y., Fu, L., Dai, S., Collu, M., Cui, L., Yuan, Z., Incecik, A., 2022. Experimental and numerical analysis of a hybrid WEC-breakwater system combining an oscillating water column and an oscillating buoy. Renew. Sustain. Energy Rev. 169, 112909. http://dx.doi.org/10.1016/j.rser.2022.112909.

Cheng, Y., Hu, Y.-N., Du, W.-M., 2026. Wave energy extraction from a floating flexible spindle-shaped wave energy converter. China Ocean Eng. 259, 2191–8945. http://dx.doi.org/10.1007/s13344-026-0059-4.

Cheng, Y., Liu, W., Dai, S., Yuan, Z., Incecik, A., 2024. Wave energy conversion by multi-mode exciting wave energy converters arrayed around a floating platform. Energy 313, 133621. http://dx.doi.org/10.1016/j.energy.2024.133621.

Cummins, W.E., 1962. The impulse response function and ship motions. Tech. Rep., (1661), David Taylor Model Basin.

Dixon, S.L., Hall, C.A., 2013. Fluid Mechanics and Thermodynamics of Turbomachinery, Seventh ed. Butterworth-Heinemann, Oxford.

Evans, D.V., 1982. Wave-power absorption by systems of oscillating surface pressure distributions. J. Fluid Mech. 114, 481–499. http://dx.doi.org/10.1017/S0022112082000263.

Falcão, A.F.O., 2010. Wave energy utilization: A review of the technologies. Renew. Sustain. Energy Rev. 14 (3), 899–918. http://dx.doi.org/10.1016/j.rser.2009.11.003.

Falcão, A.F.O., Henriques, J.C.C., 2014. Model-prototype similarity of oscillating-water-column wave energy converters. Int. J. Mar. Energy 6, 18–34. http://dx.doi.org/10.1016/j.ijome.2014.05.002.

Falcão, A.F.O., Henriques, J.C.C., 2016. Oscillating-water-column wave energy converters and air turbines: A review. Renew. Energy 85, 1391–1424. http://dx.doi.org/10.1016/j.renene.2015.07.086.

Falcão, A.F.O., Henriques, J.C.C., 2019. The spring-like air compressibility effect in oscillating-water-column wave energy converters: Review and analyses. Renew. Sustain. Energy Rev. 112, 483–498. http://dx.doi.org/10.1016/j.rser.2019.04.040.

Falcão, A.F.O., Henriques, J.C.C., Gomes, R.P.F., Portillo, J.C.C., 2022. Theoretically based correction to model test results of OWC wave energy converters to account for air compressibility effect. Renew. Energy 198, 41–50. http://dx.doi.org/10.1016/j.renene.2022.08.034.

Falcão, A.F.O., Justino, P.A.P., 1999. OWC wave energy devices with air flow control. Ocean Eng. 26 (12), 1275–1295. http://dx.doi.org/10.1016/S0029-8018(98)00075-4.

Falcão, A.F.O., Sarmento, A.J.N.A., Gato, L.M.C., Brito-Melo, A., 2020. The Pico OWC wave power plant: Its lifetime from conception to closure 1986–2018. Appl. Ocean Res. 98, 102104. http://dx.doi.org/10.1016/j.apor.2020.102104.

Fox, B.N., Gomes, R.P.F., Gato, L.M.C., 2021. Analysis of oscillating-water-column wave energy converter configurations for integration into caisson breakwaters. Appl. Energy 295, 117023. http://dx.doi.org/10.1016/j.apenergy.2021.117023.

Giorgi, G., Penalba, M., Gomes, R.P.F., 2021. Code-to-code nonlinear hydrodynamic modelling verification for wave energy converters: WEC-Sim vs. NLFK4ALL. In: Proceedings of the 14th European Wave and Tidal Energy Conference, Plymouth, UK. pp. 1971–1, 7.

Gomes, R.P.F., Henriques, J.C.C., Gato, L.M.C., Falcão, A.F.O., 2020. Time-domain simulation of a slack-moored floating oscillating water column and validation with physical model tests. Renew. Energy 149, 165–180. http://dx.doi.org/10.1016/j.renene.2019.11.159.

Gomes, R.P.F., Lopes, M.F.P., Henriques, J.C.C., Gato, L.M.C., Falcão, A.F.O., 2015. The dynamics and power extraction of bottom-hinged plate wave energy converters in regular and irregular waves. Ocean Eng. 96, 86–99. http://dx.doi.org/10.1016/j.oceaneng.2014.12.024.

Holthuijsen, L.H., 2007. Waves in Oceanic and Coastal Waters. Cambridge University Press.

Hu, Y., Cheng, Y., Dai, S., Yuan, Z., Incecik, A., 2026. Hydroelastic performance of a flexible pontoon-type floating breakwater embedded with multiple oscillating-water-column devices. Renew. Energy 259, 125065. http://dx.doi.org/10.1016/j.renene.2025.125065.

Idelchik, I.E., 2008. Handbook of Hydraulic Resistance, third ed. JAICO Publishing, House, Mumbai.

Iturrioz, A., Guanche, R., Armesto, J.A., Alves, M.A., Vidal, C., Losada, I.J., 2014. Time-domain modeling of a fixed detached oscillating water column towards a floating multi-chamber device. Ocean Eng. 76, 65–74. http://dx.doi.org/10.1016/j.oceaneng.2013.11.023.

Kurnia, R., Ducrozet, G., 2021. NEMOH v3.0 User Manual, École Centrale de Nantes. http://dx.doi.org/10.13140/RG.2.2.12752.28162.

Lee, C.H., Newman, J.N., 2021. WAMIT User Manual. https://www.wamit.com/version7.0.htm.

National Renewable Energy Laboratory and Sandia National Laboratories, 2022. WEC-Sim v6.0 Theory Manual. https://wec-sim.github.io/WEC-Sim/dev/theory/index.html.

Ogilvie, T.F., 1964. Recent progress toward the understanding and prediction of ship motions. In: Proceedings of the 5th Symposium on Naval Hydrodynamics, Bergen, Norway. pp. 3–80.

Oikonomou, C.L.G., Gomes, R.P.F., Gato, L.M.C., 2021. Unveiling the potential of using a spar-buoy oscillating-water-column wave energy converter for low-power stand-alone applications. Appl. Energy 292, 116835. http://dx.doi.org/10.1016/j.apenergy.2021.116835.

Portillo, J.C.C., Gato, L.M.C., J.C.C. Henriques, A.F.O. Falcão, 2023. Implications of spring-like air compressibility effects in floating coaxial-duct OWCs: Experimental and numerical investigation. Renewble Energy 212, 478–491. http://dx.doi.org/10.1016/j.renene.2023.04.143.

Ruehl, K., Keester, A., Tom, N., Forbush, D., Grasberger, J., Husain, S., Ogden, D., Leon, J., 2023. WEC-Sim v6.0. http://dx.doi.org/10.5281/zenodo.10023797.

Ryan, S., Algie, C., Macfarlane, G., Fleming, A., Penesis, I., King, A., 2015. Assessing the global wave energy potential the Bombora wave energy converter: A novel multi-purpose device for electricity, coastal protection and surf breaks. In: Proceedings of the Australian Coasts and Ports 2015: 22nd Australasian Coastal and Ocean Engineering Conference and the 15th Australasian Port and Harbour Conference, Auckland, New Zealand, Engineers Australia. pp. 541–546.

Scialò, A., Henriques, J.C.C., Malara, G., A.F.O. Falcão, L.M.C. Gato, Arena, F., 2021. Power take-off selection for a fixed U-OWC wave power plant in the Mediterranean Sea: The case of Roccella Jonica. Energy 215, 119085. http://dx.doi.org/10.1016/j.energy.2020.119085.

So, R., Bosma, B., Ruehl, K., Brekken, T.K.A., 2020. Modeling of a wave energy oscillating water column as a point absorber using WEC-Sim. IEEE Trans. Sustain. Energy 11 (2), 851–858. http://dx.doi.org/10.1109/TSTE.2019.2910467.

Tedd, J., Kofoed, J.P., 2009. Measurements of overtopping flow time series on the Wave Dragon wave energy converter. Renew. Energy 34, 711–717. http://dx.doi.org/10.1016/j.renene.2008.04.036.

Uihlein, A., Magagna, D., 2016. Wave and tidal current energy - a review of the current state of research beyond technology. Renew. Sustain. Energy Rev. 58, 1070–1081. http://dx.doi.org/10.1016/j.rser.2015.01.061.